THESIS

INVESTIGATING AND MITIGATING ERRORS IN THE REMOTE SENSING OF MARITIME LOW CLOUDS AT NIGHT

Submitted by

Jesse Turner

Department of Atmospheric Science

In partial fulfillment of the requirements

For the Degree of Master of Science

Colorado State University

Fort Collins, Colorado

Fall 2024

Master's Committee:

Advisor: Steven D. Miller

Christian D. Kummerow
Ryan G. Smith
Yoo-Jeong Noh

ABSTRACT

INVESTIGATING AND MITIGATING ERRORS IN THE REMOTE SENSING OF MARITIME LOW CLOUDS AT NIGHT

Low clouds are ubiquitous to the world's oceans, affecting aviation, maritime transportation, and the structure and dynamics of the broader atmospheric system. Understanding the diurnal properties and distributions of these clouds requires an observing system capable of spanning vast regions of ocean devoid of surface-based observations. Here, earth observation satellite imagery provides potentially valuable information on cloud coverage over the oceans.

The brightness temperature difference (BTD) between the longwave infrared (e.g., 11 μm) and shortwave infrared (e.g., 3.9 μm) window band measurements is commonly used as a first-order bi-spectral test to identify low clouds over the ocean at night. Occasionally, unusual patterns of clear-sky features in this BTD occur, giving rise to spurious false-positive cloud measurements. These confusing signals are caused by nuances of the atmospheric and surface emission sensitivity at these two wavelengths. Ideally, positive values in the 11 μm - 3.9 μm BTD are caused by actual low clouds, owing to slightly higher emissivity at the longwave IR compared to the shortwave IR. However, a clear-sky environmental scenario can mimic this signal: a warm and moist air mass over a cold region of water. These same environmental conditions are conducive to advection fog formation, compounding the interpretation of conventional infrared-based cloud detection in these regions. Moonlight reflectance, when available from the Day/Night Band on the Visible/Infrared Imaging Radiometer Suite (VIIRS), can help to disentangle cases of actual vs. false low cloud (FLC).

This research examines cases from the United States east coast, the Mexico south coast, and the large-scale Gulf Stream to investigate the physical causes of false cloud signals. Insight gained from this research can help forecasters and researchers determine which physical regions are prone

to false alarms, and in complement, which regions offer higher confidence for cloud detection. Further, this study uses numerical model data and radiative transfer simulations to estimate the positive signals caused solely by air mass over cold water effects. This simulation method lends insight on the global extent and frequency of nighttime maritime low cloud overstatement. Knowledge of the patterns of false signals in the IR BTD provides opportunities to improve products that depend on the nighttime low cloud test, such as fog and visibility warnings, sea-surface temperature cloud masking, and cloud climatologies used for climate research. The simulation also provides a novel predictive tool for anticipating potential regions of both false alarm low cloud and regions prone to advection fog formation.

ACKNOWLEDGEMENTS

I would like to thank my advisor, Prof. Steve Miller for giving me the opportunity to work with him and the excellent teams at Colorado State University and the Cooperative Institute for Research in the Atmosphere. Steve has helped me at every step as I worked on this project, and provided an ideal environment for novel ideas and effective science. Steve also organized a wonderful research group, every member of which has been important to this work. I would also like to thank Prof. Christine Chiu, Dr. Yoo-Jeong Noh, and Bill Line. Christine was instrumental in helping me get started in this field, and I would not have been able to find my footing without her. She also lent her expertise in the radiative transfer modeling section, where she guided me in the use of the water vapor absorption coefficients. Yoo-Jeong has been my voice of reason throughout this project, keeping the science fundamentally sound and the scope balanced between ambition and practicality. Much of what I've learned, and continue to learn, about proper science methodologies comes directly from her. Bill Line has also long been one of my biggest sources of support in this field, and I so appreciate his constant kindness and generosity. Additionally, I am grateful to Prof. Chris Kummerow and Prof. Ryan G. Smith for being alongside me and offering their valuable perspectives to this research. Lastly, I would like to thank the rest of the incredible people at CIRA and CSU, for being part of this community which has been so meaningful to me.

TABLE OF CONTENTS

LIST OF FIGURES

Chapter 1

Introduction

1.1 Importance of accurate low cloud sensing

Accurate and complete characterization of meteorological cloud fields is integral to both climate studies and weather operations (Hartmann, 2016; Wood, 2012). Satellite remote sensing provides a useful platform for monitoring oceanic clouds due to the limited reach of ground-based sensors. The validity of the measured extent of low clouds over the ocean is important because errors can lead to forecasting difficulties and the contamination of data used for atmospheric research. The global cloud field follows a diurnal cycle, which has direct effects on the Earth's energy budget (Bergman and Salby, 1997), and this makes it essential for the measurement of cloud extent to be accurate during both day and night.

Throughout this study, the terms "marine boundary layer (MBL) clouds", "low clouds", and "fog" will be used interchangeably. For our purposes, all refer to suspended water droplets with cloud top temperatures similar to the surface temperature (Torregrosa et al., 2016). Fog and low clouds can differ in their base height, methods of formation, and patterns of transportation. However, passive radiometers aboard satellites measure information near the cloud tops, making it difficult to determine if the bases of low clouds are lofted or at the surface (Noh et al., 2022). Since the global low cloud field is made up of both surface-contacting fog and lofted low clouds, we do not distinguish between them in this research.

MBL clouds include fog, stratocumulus, stratus, and cumulus clouds over the ocean. The accurate measurement of MBL clouds is climatically important in the daytime because they reflect solar radiation that would otherwise be absorbed by the relatively dark ocean. Low clouds, including MBL clouds, are shown to make the largest average contribution to the net energy balance of the Earth (Hartmann et al., 1992). MBL clouds have an albedo of 0.4 to 0.8, as opposed to the sea

surface albedo of 0.05 to 0.1. During the day, MBL clouds have a net cooling effect on the global climate due to the increase in reflectivity at the surface (Hartmann, 1992).

At night, MBL clouds play an active role in the dynamics of the boundary layer and the surface. When there is no sunlight to reflect, MBL clouds warm the surface by re-emitting infrared (IR) radiation downward (Hartmann, 2016; Liou, 2002; Petty, 2006). During the night, cloud top radiative cooling drives MBL clouds to deepen and the liquid water path to increase, making them more likely to form precipitation (Dong et al., 2014).

The dynamics of MBL clouds have been shown to be the main source of uncertainty in climate models (Bony and Dufresne, 2005). There is ongoing investigation into how warming sea temperatures will effect the MBL coverage (Zhou et al., 2021). In order to understand the intricacies of the effects of MBL clouds on radiative feedbacks and Earth's energy budget, it is necessary to improve satellite measurement of the MBL cloud distribution, accounting for both day and night.

Accurate measurement of marine boundary layer clouds is also important for understanding global light precipitation. Warm rain from low clouds is an integral part of the tropical hydrological cycle and contributes to the heating and moistening of the lower troposphere (Lau and Wu, 2003). 20% of total rainfall over the tropical oceans is from low clouds (Duncan et al., 2018).

Maritime low clouds are also important to forecasters, due to the weather hazards they present. The impact on visibility at the near-surface has effects on visual flight rules aviation and marine operations. Low ceilings and low cloud layers are attributed to the majority of fatal accidents in aviation (Fultz and Ashley, 2016). Maritime search and rescue operations are significantly hampered by low clouds. Marine fog also has implications on Department of Defense operations, where it impairs visibility and hampers directed-energy weapons (Tracey, 2016).

Beyond the measurement of MBL clouds themselves, sea surface temperature (SST) datasets generated with remote sensing rely on effective cloud masks to determine which pixels represent SST and which represent cloud temperature (McClain et al., 1985; Petrenko et al., 2010). These datasets drive large areas of research, including climate models and oceanic studies. Errors in low cloud sensing are inherited into cloud masking, and passed along to the users of SST datasets.

Marine fog and low clouds are known to be particularly difficult to predict, as they can appear very quickly (Koračin and Dorman, 2017). Even a marginal increase in the accuracy of maritime low cloud coverage sensing could have far-reaching effects. Given the range challenges of sensing clouds from surface based systems, satellite remote sensing is generally used for MBL cloud extent. In particular, geostationary satellites offer the additional advantages of high temporal resolution over a large area of the world and a consistent angle of view. However, the satellite methods are not perfect, and it is important to understand the capabilities and limitations of the retrieved MBL cloud coverages. This research explores the challenges and potentials of MBL cloud detection at night from the satellite platform.

1.2 Remote sensing of low clouds at night

During the day, many cloud features are readily visible from reflected visual-spectrum (e.g., ~0.65 μm band) imagery. If the surface is sufficiently low albedo (such as over the ocean), the relatively high albedo of the clouds allows them to be easily differentiated through reflectance contrast. This capability tends to fail when differentiation is needed between higher and lower clouds, where thermal IR information becomes useful for cloud height assignment. Challenges also occur when differentiating between clouds over snow and ice. For these cases, sometimes the reflected solar component of the shortwave IR band centered at about 3.9 μm can be used to distinguish the low clouds. This is done by taking advantage of the higher reflectance of 3.9 μm from water droplets, as compared to ice clouds or snow (Lee et al., 1997) which are more absorptive.

At night, cloud detection involves measuring thermal contrast in the IR spectrum. This is done by calculating the equivalent brightness temperature from the radiance observed from the satellite. For clouds that are sufficiently high and cold, there is a significant contrast between their brightness temperature and that of the underlying surface. An inversion of Planck's Law [Equation (2.5)] can be used to estimate the brightness temperature, given an observed radiance and the inherent assumption of a blackbody emitter. Departures from this assumption provide differences

in brightness temperatures for scenes observed at different spectral bands, giving rise to the signals of interest to this research.

The thermal gross contrast tests can often be sufficient for nighttime detection of high and cold clouds over relatively warm surface backgrounds. However, low clouds emit at a similar temperature to the surface, making them less distinguishable via these methods. In order to visualize these warmer low clouds at night, slight differences in cloud spectral emissivity between IR wavelengths can be exploited. Smaller cloud drops, with droplet size distribution effective radii of around 8-12 μm, tend to occur in these boundary layer clouds (Hansen and Travis, 1974). At longwave IR wavelengths (e.g., 11 μm) the emissivity of these droplets are close to that of a blackbody (~1), and thus the brightness temperature of these clouds are similar to that of their thermodynamic cloud top temperature. However, the emissivity of these same droplets at shortwave IR wavelengths (e.g., 3.9 μm) is less ($\varepsilon < 1$, with smaller values for smaller droplets (Hunt, 1973). Liquid-phase clouds therefore produce radiometrically cooler brightness temperatures in the 3.9 μm band than in the 11 μm band. By taking a pixel-by-pixel brightness-temperature difference (BTD) between longwave and shortwave IR wavelengths, low clouds can be differentiated from the underlying surface if that surface does not exhibit a similar spectral emissivity behavior to that of the clouds (Ellrod, 1995). Throughout this work, the "longwave IR" will refer to any wavelength from 10.3 μm to 12 μm. The "shortwave IR" will refer to any wavelength from 3.7 μm to 3.9 μm. The nighttime low cloud test generated from the longwave IR - shortwave IR BTD will simply be referred to as the "IR BTD".

Figure 1.1 shows an average of IR BTD in January 2023, from the Advanced Baseline Imager (ABI) aboard GOES-16, the first satellite of the Geostationary Operational Environmental Satellites (GOES) R-series. In many satellite imagery products, including satellite-derived fog and low cloud climatologies, the IR BTD method is directly used to determine the nighttime low cloud field (Torregrosa et al., 2016). The average IR BTD in Figure 1.1 was made by limiting BTD to the positive (which generally means low cloud measurement) and collecting a snapshot from each night at 06:00 UTC. Negative IR BTD measurements are usually associated with clear sky or high

clouds, and were not included in this composite image. Note the strong positive IR BTD signal off the coast of Chile, which is representative of the MBL clouds that tend to exist in the region.

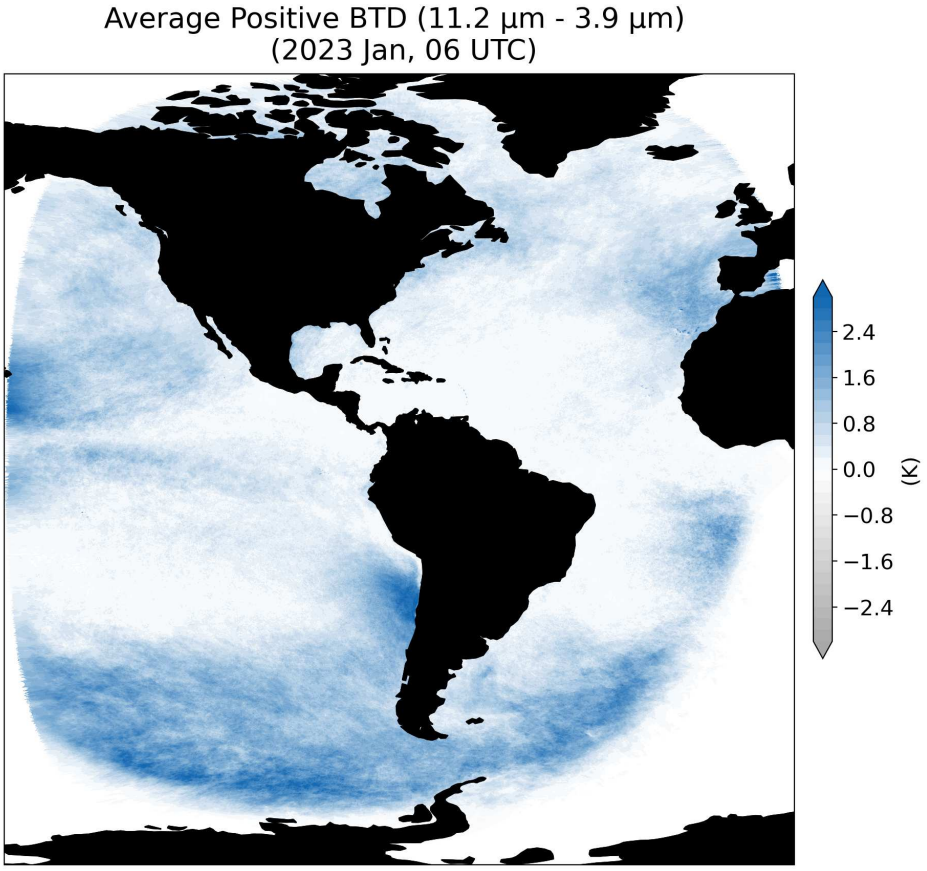

Figure 1.1: The average positive IR BTD as measured by GOES-16 ABI during the month of January 2023. The data was collected each day at 06:00 UTC, which is nighttime for most of the Western Hemisphere. Note that some of the well-known MBL cloud decks are visible, including off the coast of Chile.

The shortwave IR bands used for the nighttime low cloud test do not work during the day. The band is unique in being sensitive to both emitted terrestrial radiation and reflected solar radiation. During the day, the reflected solar radiation causes the shortwave IR to measure much warmer than the longwave IR, nullifying the effectiveness of the IR BTD. A consequence of this is that the IR BTD results cannot usually be directly compared to a visible-spectrum low cloud field.

The IR BTD has known limitations in the detection of low clouds at night. In maritime environments with particularly clean air, low clouds often have larger cloud top particle sizes and the

IR BTD signal is weaker (Ellrod, 1995). Thin cirrus has high transmissivity in the shortwave IR and appear warmer than in the longwave IR. Therefore, cirrus clouds overriding low clouds causes the IR BTD to reverse and measure a negative result. Equivalently, the ice crystals in the high clouds absorb much more in the longwave IR.

Another known limitation of detecting nighttime MBL clouds with the IR BTD is that cloud-free regions can still result in a small positive due to differential water vapor absorption. This last phenomenon is the focus of this research.

The IR BTD works, in part, due to the lack of scattering at these IR wavelengths. If the air molecules (nitrogen, oxygen, water vapor) scattered in the thermal IR (as occurs in the visible spectrum), the radiation at either or both of the IR bands would be diffused throughout the atmosphere. However, for wavelengths longer than 3 μm, the air molecules are comparatively small enough that there is a negligible effect on the radiation intensity (Kopeika et al., 2014). Another factor that makes it plausible to compare the longwave IR and shortwave IR is because they both exist in "atmospheric windows". The atmosphere is largely transparent (not quite) to radiation at these wavelengths, meaning that a satellite sensor tuned to these will detect emission from near the surface of the earth. If this were not the case and the satellite weighting function was much higher in the atmosphere, then low clouds would be invisible simply due to being below the emissive levels. However, the catch is that these two windows are not entirely clean, and this can cause complications in the IR BTD.

1.3 Errors in the IR BTD

Previous research shows that infrared-based cloud detection techniques miss nighttime clouds over the ocean at a rate of about 7% (Heidinger et al., 2012). The global rate of cloud overstatement during the night is less well known. In a few recent studies, attempts have been made to investigate physical environmental conditions and improve the rates of cloud detection at night, including methods that reduce both the false positive and false negative detection rates. For instance, steep gradients in SST are known to produce overstatements of the cloud field, their identification and

mitigation stand to improve the overall cloud assessment (Petrenko et al., 2010). However, satellite products dependant on the IR BTD have found no simple algorithmic adjustment that will rid them of false positives without significant loss of cloud detection probability (Gladkova et al., 2015). This research attempts to circumvent errors in the nighttime cloud measurements by recognizing the patterns of false low cloud (FLC) signals.

Studies have shown that the overstatement of clouds signals in the infrared BTD tends to occur near strong SST gradients such as coastal zones, river outflows, and ocean banks (Miller et al., 2022). These nighttime false cloud signals can often be identified visually by their persistently unchanging shape and a distinctive outline (Gladkova et al., 2015). Investigation into the infrared bands has linked these false positives to physical phenomena that involve warm, moist air overriding cold water (Miller et al., 2022). This effect is due to the differing absorption to water vapor between the longwave IR and the shortwave IR. In a cloud-free atmosphere, the shortwave IR experiences less atmospheric contributions from water vapor than the "dirtier" longwave IR bands. For the two longwave infrared window bands on the ABI sensor centered at 10.35 μm and 11.2 μm, the latter is situated in part of the atmospheric absorption spectrum that experiences more water vapor absorption. This distinction is shown in Figure 1.2. However, the ABI shortwave IR band centered at 3.9 μm experiences less atmospheric vapor absorption, such that almost all signal comes from the surface. When these values are converted to brightness temperature, the longwave bands are disproportionately affected by moist air compared to the shortwave bands. A warm and moist air mass over a colder ocean surface therefore can have a very similar IR BTD signal to low level clouds.

In order to solidify this relationship between physical variables and positive signals in the satellite-measured IR BTD, simulations were run using the Santa Barbara DISORT Atmospheric Radiative Transfer (SBDART) model (Ricchiazzi et al., 1998). The SBDART software computes plane-parallel radiative transfer within the atmosphere and allows for customization of cloudy or clear scenarios, different regions, and seasons. We used SBDART settings for a US standard atmosphere, with clear sky (no clouds), solar zenith angle of >180° (nighttime) and a location of

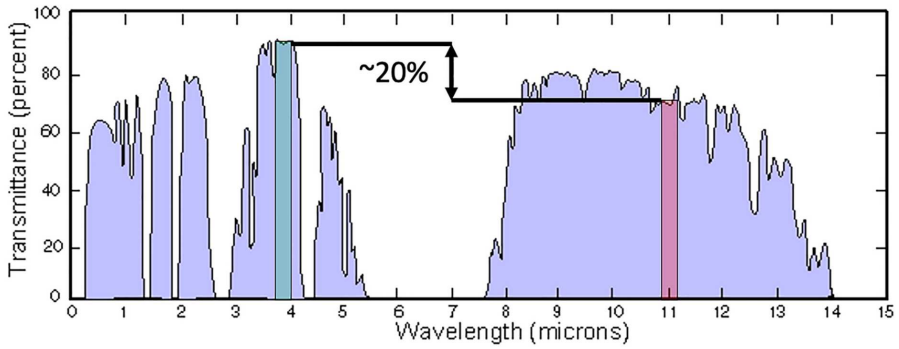

Figure 1.2: Spectral transmission through the atmospheric column, highlighting the difference in longwave and shortwave infrared absorption. Adapted from Miller et al. (2022). Copyright 2022 by the American Geophysical Union, Earth and Space Science.

41° N, -68° W (off the coast of Massachusetts). We varied the inputs of SST and precipitable water vapor to determine if atmospheric moisture over a cold SST could cause a positive IR BTD signal. In Figure 1.3, the SBDART simulation shows that this positive can occur from these variables on a clear sky night, which further supports the evidence for the FLC environment described.

Previous studies have acknowledged the difficulty of differentiating certain SST patterns from clouds (Gladkova et al., 2015). These patterns are generally contiguous, with well-defined boundaries, and often located near ocean thermal fronts. The Gulf Stream has been noted as a region of particular confusion, where automated cloud detection algorithms frequently overstate the cloud-covered area. Despite the difficulty for automated systems, the distinctions between true and false cloud are usually quite evident when visually evaluated by an expert. Gladkova et al. (2015) presents a test that uses the SST gradient information, spatial connectivity, and frequencies of patterns to identify regions that will likely be erroneously marked as cloudy in operational satellite cloud products that use the IR BTD.

There are a few alternative methods for detecting low clouds at night, beyond the use of the IR BTD. The Day/Night Band (DNB) is a visible/near-IR sensor capable of resolving clouds using reflected moonlight in the visible spectrum. This instrument is aboard polar-orbiting satellites, and therefore lacks the temporal resolution of the GOES-based IR BTD. Another limitation is that the DNB requires sufficient moonlight to effectively measure cloud extent, and is only useful for

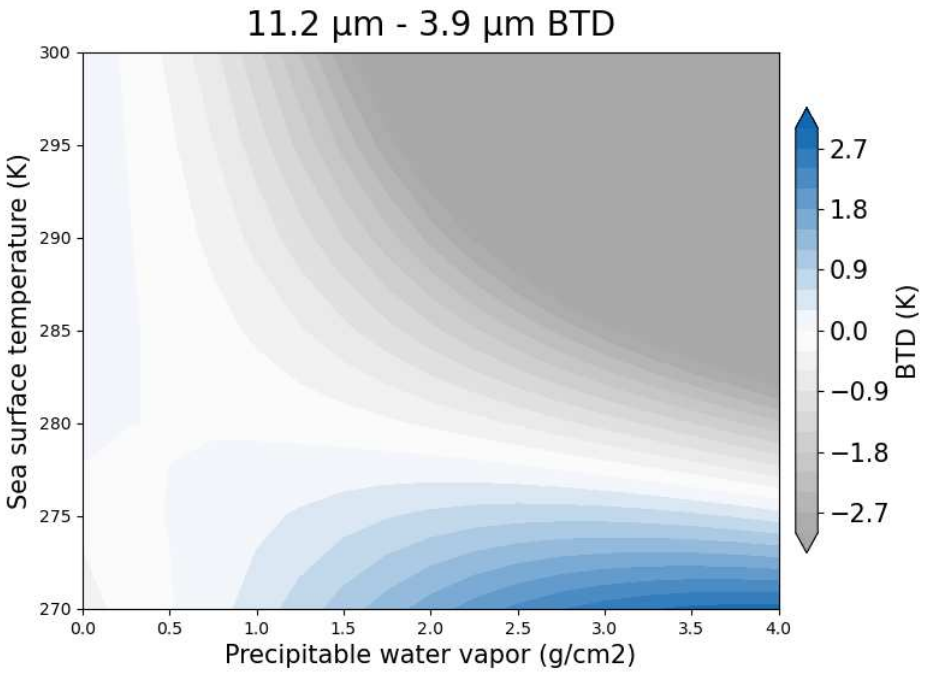

Figure 1.3: A simulation of the 11.2 µm – 3.9 µm brightness temperature difference using the Santa Barbara DISORT Atmospheric Radiative Transfer (SBDART) model. Increasing the moisture in the atmosphere increases the difference between the longwave IR and the shortwave IR, due to their differing sensitivities to water vapor. A false cloud signal is simulated when moist air is overriding a relatively cold surface temperature.

differentiating FLCs from true clouds during certain phases of the lunar cycle. This research uses DNB imagery as additional evidence for FLC events. More details on the methods for using DNB imagery in this research are in Chapter 2.2.

Lidar observations can also detect nighttime low clouds. For the goal of measuring maritime clouds far from land, space lidar is likely necessary. Data from the Cloud-Aerosol Lidar and IR Pathfinder Space Observation (CALIPSO; Winker et al., 2009) mission has been leveraged in the past to determine the accuracy of positive measurements in the IR BTD (Miller et al., 2022). The Cloud-Aerosol Lidar with Orthogonal Polarization (CALIOP) instrument aboard CALIPSO is effective at detecting MBL clouds at night, but the lidar curtain does nothing to determine the horizontal extent of cloud coverage (Winker et al., 2009).

1.4 Satellite products that use the IR BTD

Many products rely on the IR BTD to detect low clouds at night. For example, satellite-derived SST products will use the IR BTD as part of a cloud masking algorithm (Petrenko et al., 2010). Overstatements in the nighttime cloud extent can put these products at risk of inheriting errors and developing biases. Some regions are particularly prone to FLC signals, due to the frequent existence of warm moist air over colder waters. Forecasters rely on imagery produced using these methods, and errors can have effects on maritime transportation and aviation. Understanding the patterns of the false cloud signals from different physical causes can help identify regions which experience this issue. The simulation of the water vapor effects in the IR BTD can be used as a warning for when and where the nighttime MBL cloud extent may be overstated.

Climatologists also use products dependent on the IR difference to gauge historical marine low cloud extent. When the low cloud field is overstated, it causes reoccurring issues in those records. Additionally, SST climatologies generated by satellite data often have to filter out cloud-covered regions. The possible overstatement of low cloud in regions where cold SSTs occur in conjunction with warm moist overriding air could filter out valid SSTs. This errant filtering can lead, in turn, to a regional warm bias in the SST data record, especially when considering that

nighttime SSTs are used to produce these climatological records (which do-so to avoid significant variability in daytime solar-heating skin temperature effects; Pimentel et al., 2018). In order to make the nighttime MBL cloud record as accurate as possible, it is necessary to know the global false positive rates in the infrared low cloud test.

GeoColor, developed by the Cooperative Institute for Research in the Atmosphere (CIRA), is a multispectral data product offering the combination of true-color imagery during the day and an infrared product at night (Miller et al., 2020). GeoColor uses multidimensional blending to display multiple pieces of distilled information simultaneously. In the vertical dimension at night, GeoColor combines a single-band IR high cloud layer with an IR BTD low cloud layer. For the GOES ABI GeoColor product, the IR BTD uses 10.3 μm - 3.9 μm BTD normalized between [0.0K, 4.0K] over the ocean.

The Advanced Clear-Sky Processor for Oceans (ACSPO) Clear-Sky Mask is frequently used for SST datasets. The product uses a similar infrared difference method for their low cloud field, referred to as the "Three minus five test" or the "Uniform low stratus test" (Petrenko et al., 2010). The ACSPO was designed for the Advanced Very High Resolution Radiometer (AVHRR/3), and uses thermal infrared bands centered at 3.7 μm (Band 3) and 12 μm (Band 5). It has since been extended to other sensors, including the Moderate Resolution Imaging Spectroradiometer (MODIS) aboard Terra and Aqua satellites and the ABI.

The ProxyVis product is constructed from longwave and shortwave IR channels to visualize tropical cyclone low-level circulation centers at night (Chirokova et al., 2023). ProxyVis is very successful in creating synthetic visible imagery at night, but experiences false cloud signals in regions of sharp SST gradients at higher latitudes. Figure 1.4 shows an example of a region where the IR methods show cloud cover and the DNB visible imagery shows clear sky. Forecasters have noted that these SST features are easy to distinguish from clouds in animations, where there is a visual difference between clouds and SST features in the time evolution.

The accuracy of the measurement of the MBL cloud field has strong impacts on climate models and the data record. Many products used by forecasters rely on the IR BTD and are therefore

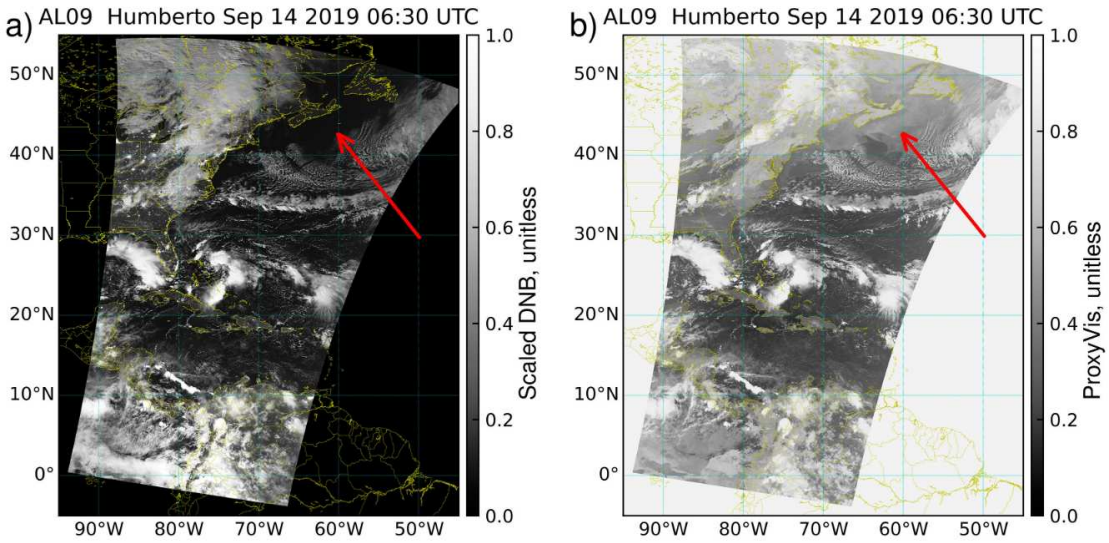

Figure 1.4: Comparison of (a) VIIRS DNB and (b) ProxyVis for VIIRS data, showing the overstatement of clouds in the IR-dependent ProxyVis product. Lighter colors are cloud coverage. Adapted from Chirokova et al. (2023). Copyright 2023 by the American Meteorological Society, Journal of Weather and Forecasting.

hindered by FLC features. These issues have been acknowledged, but the extent and temporal patterns of the FLC signals is largely unknown. This work attempts to determine some physical patterns, and presents a method for the simulated isolation of the false signals. This knowledge could improve the usability of all the dependent products (GeoColor, ACSPO, ProxyVis, etc.), and the accuracy of the measurement of nighttime MBL clouds.

1.5 Goals of this study

This research aims to investigate the physical causes and patterns of false nighttime cloud signals in satellite observations, and present a method using numerical model data and radiative transfer simulations to quantitatively estimate the effects of atmospheric and oceanic conditions that can lead to FLC signals in satellite data. These steps are carried out with the goal of improving our understanding and supporting more accurate nighttime cloud detection.

The known general conditions of warm and moist air over cool SSTs described by Miller et al. (2022) can be realized by a range of natural phenomena. While specific examples have been presented anecdotally, a deep dive of the underpinning physical processes and their distribution

and frequency of occurrence in nature has not been conducted. Thus, the driving science questions of this research are:

1. **What are the specific underpinning physical processes of these various phenomena?**

   We hypothesize that the circumstances giving rise to the FLC signal will occur from a variety of physical processes, including air-sea interactions. We address this hypothesis by identifying FLC cases and investigating in detail the coincident physical scenario (winds, topography, meteorological analyses, etc.) with ancillary data.

2. **Where, when, and how do these FLC processes occur in nature?**

   We hypothesize that these processes will be tied to local regional and seasonal conditions that tend to create cold SST under warm and moist air masses. By using prior knowledge of the regions and composite imagery analyses of positive IR BTD, we test our hypothesized relationship against the true regional patterns of moisture, air temperature, and SST.

3. **To what extent can we anticipate the development of these processes globally?**

   We hypothesize that a quantitative simulation of the positive IR BTD signal tied to a global numerical model analysis of atmospheric temperature/moisture profiles and SST can reveal the regions globally that produce the FLC phenomenon. To explore this question, we will simulate the FLC signals by way of numerical model data and basic radiative transfer modeling to locate positive IR BTD signals caused solely by water vapor over cold surface effects, and compare these results to the satellite-observations.

In addressing Science Questions 1 and 2, intensive case studies were carried out for a variety of regions to investigate the atmospheric moisture and temperature structures associated with FLC events. These deep-dives include locations along the United States east coast, the Mexico south coast, the large-scale Gulf Stream, and physical scenarios such as ocean banks, gap-winds off the coast, and large-scale ocean currents. The results of these studies are detailed in Chapter 3.

The simulated version of the IR BTD, enabling pursuit of Science Question 3, is developed in Chapter 4. This method requires numerical model data to provide atmospheric temperature

and moisture, and requires SST data to provide surface temperatures. This FLC simulation also offers insight into how we can effectively remove false signals from satellite imagery, creating a more accurate low cloud field over the ocean. Furthermore, it provides a novel predictive tool for anticipating potential regions of both false alarm low cloud and regions prone to advection fog formation.

Knowledge gleaned from this research holds potentially high value for both forecasters and researchers alike in terms of evaluating the reliability of cloud and SST assessments for a specific region and time. Specifically, insights and predictive tools from this research can help forecasters and researchers determine which physical regions are prone to maritime low-cloud false alarms and under what driving conditions. In complement, these same tools help to determine which regions offer higher confidence for cloud detection. Additionally, this research could help enhance the accuracy of the satellite-derived climatologies of nighttime MBL clouds and thereby improve the usability of satellite cloud observations and downstream products that are dependent on accurate cloud masks for various weather and climate studies.

Chapter 2

Data and Methodology

This section provides explanations of the sources of data and processes used in this study. GOES satellite data makes up the bulk of the observations in Chapter 3. The FLC simulation, described in Section 2.6, is built from Global Forecast System (GFS) data (Section 2.3), National Oceanic and Atmospheric Administration (NOAA) SST data (Section 2.4), and high-resolution transmission molecular absorption database (HITRAN) molecular absorption data (Section 2.5).

2.1 GOES-R Advanced Baseline Imager data

The GOES series of satellites provides imagery via the ABI instrument (Schmit et al., 2017; Kalluri et al., 2018). The ABI possesses 16 bands, ranging from the visible to the infrared. At nadir, the resolution ranges from 0.5 km to 2 km. Temporal resolution is generally 10 min, but is at a higher resolution of 30 s within certain mesoscale regions. GOES-R is currently made up of two satellites, GOES-16 (GOES-East; to be replaced by GOES-19 in 2025) and GOES-18 (GOES-West). Both fly over the equator, with GOES-East at 75.2°W and GOES-West at 137°W.

GOES-R data is available the Registry of Open Data on Amazon Web Services (https://registry.opendata.aws/noaa-goes/). The data is returned on a scan angle (x,y) grid, and the pixels needed to be converted into latitude and longitude grid in order to be directly compared to most geological data (such as coastlines). This was done using the GOES imager projection metadata included in the file, and Equation (2.1) & (2.2). These equations were inspired by Hrisko (2018).

$$\phi = \arctan\left(\frac{r_{eq}^2}{r_{pol}^2}\frac{s_z}{\sqrt{(H-s_x)^2+s_y^2}}\right) \tag{2.1}$$

$$\lambda = \lambda_0 - \arctan\left(\frac{s_y}{H-s_x}\right) \tag{2.2}$$

- r_{eq} = radius of Earth at the equator

- r_{pol} = radius of Earth at the pole
- H = distance from satellite to earth center
- λ_0 = longitude of projection origin
- s_x, s_y, s_z = derived using satellite location and earth geometry

GOES-R data is returned as the radiance measured by each ABI sensor. In order to compare directly between two bands, centered over two different wavelengths, the radiance measurements are converted to brightness temperatures. Equation (2.5) shows the inversion of the Planck Function that converts the observed radiance to brightness temperature.

$$B_\lambda(T) = \frac{2hc^2}{\lambda^5[e^{hc/k\lambda T} - 1]} \tag{2.3}$$

$$I_\lambda = \epsilon_\lambda B_\lambda(T) \tag{2.4}$$

$$T_b = \frac{hc}{k\lambda}\ln^{-1}\left(1 + \frac{2hc^2}{I_\lambda\lambda^5}\right) \tag{2.5}$$

- $B_\lambda(T)$ = blackbody radiance at wavelength
- ϵ_λ = emissivity at wavelength
- T_b = Brightness temperature
- h = Planck constant
- c = Speed of light
- k = Boltzmann constant
- I_λ = Observed radiance at wavelength

- λ = Wavelength

  This study uses BTD between a longwave infrared band (11.2 μm, ABI band 14) and a shortwave infrared band (3.9 μm, ABI band 07).

2.2 VIIRS Day/Night Band data

The Day/Night Band (DNB) visible/near-IR bandpass radiometer is available as another way to visualize maritime cloud extent at night (Miller et al., 2013). The DNB is part of the Visible/IR Imaging Radiometer Suite (VIIRS), carried on the NOAA Joint Polar Satellite System (JPSS) Suomi National Polar-Orbiting Partnership (S-NPP), NOAA-20, and NOAA-21 satellites (Goldberg et al., 2013). The DNB is capable of resolving very low-light sensitivity, and is able to detect clouds at night using reflected visible-spectrum moonlight (nominally, down to radiance levels of ~3×10^{-5} W/m^2/sr/μm at a signal to noise ratio of ~10). However, the lunar cycle (i.e., lunar phase, ranging from New Moon to Full Moon) determines whether there is sufficient reflected radiance to visualize nighttime clouds (Miller and Turner, 2009). With sufficient moonlight, DNB imagery provides a useful complement to the infrared methods of cloud sensing at night.

DNB imagery is leveraged to differentiate FLCs from true MBL clouds in Miller et al. (2022). We use a similar method in Chapter 3. Due to the difficulty of resolving clouds in low moonlight nights, we limited case studies that used DNB comparisons to nights of >90% lunar illumination.

DNB data was downloaded from NOAA's Comprehensive Large Array-data Stewardship System (CLASS). The necessary files are the VIIRS Near Constant Contrast (NCC) EDR Ground Track Mercator (GTM) Geolocation (GNCCO) and the VIIRS Near Constant Contrast Imagery EDR (VNCCO). NCC was presented in Liang et al. (2014) as a method of making DNB data usable during all moon phases. Despite this, low clouds are still optimally visible during full moon or near full moon phases. The geolocation and data files are combined to plot individual granules against a map projection provided by the Cartopy Python package.

2.3 NOAA Global Forecast System model data

The Global Forecast System (GFS) is a weather forecast model produced by the National Centers for Environmental Prediction (NCEP). This study only used non-forecasting data, from the warm start initial conditions produced by NCEP. For initial conditions data, the GFS horizontal resolution is 1/4 degree. The GFS model was chosen due to the global coverage, and the matching resolution to the SST data. We use GFS version 16, the most current at the time of this publication. The GFS data is accessed from Amazon Web Services (https://registry.opendata.aws/noaa-gfs-bdp-pds/).

GFS data makes up one of the two inputs needed for the FLC simulation of IR emission. The variables utilized from the GFS model are air temperature and specific humidity, each having dimensions of latitude, longitude, and vertical pressure levels. We use a vertical range from 1000 hPa to 100 hPa, made up of 21 atmospheric layers. The vertical resolution is 25 hPa from 1000 hPa to 900 hPa, then coarsens to 50 hPa for the layers above 900 hPa.

2.4 NOAA Sea surface temperature data

The NOAA Daily Optimum Interpolation Sea Surface Temperature (OISST) is made up of observations from satellites, ships, buoys and Argo floats. These measurements are interpolated onto a regular global grid at 1/4 degree resolution. We use OISST version 2.1, the most current at the time of this publication. The OISST data is accessed from the National Centers for Environmental Information (NCEI).

This SST dataset was chosen due to the inclusion of surface observations. A satellite-only SST product with a cloud mask would not be effective due to most cloud masks inheriting FLC errors (which would eliminate the SSTs causing our target feature). Even an interpolated SST data product, without the addition of surface observations, would likely blend over the localized cold regions due to misrepresentation as overriding cloud. The OISST has the advantage of ships, buoys, and Argo floats to solidify these cold regions in the data. However, this is not without the potential introduction of bias. Buoy coverage is much higher density around

the coasts of North America than the rest of the world (National Buoy Data Center, NOAA; https://www.ndbc.noaa.gov). Global shipping routes also favor the coasts, along with specific defined lines across the ocean (Shipping Routes, NOAA; https://sos.noaa.gov/catalog/datasets/shipping-routes-with-labels-one-year/). Argo floats have a more spatially uniform global ocean coverage, but with resolution limited to 3960 floats (University of California San Diego; https://argo.ucsd.edu/about/status/). The factors from these data sources make it more likely for FLC events to be identified in the simulations along the coasts (particularly North America), where the surface observations are most prevalent.

2.5 HITRAN molecular absorption data

The HITRAN molecular absorption database (https://hitran.org; Gordon et al., 2022) provides a compilation of molecule-dependent transmission and emission values. These are also dependent on spectroscopic parameters such as wavenumber and spectral line shape (Lorentzian, Gaussian, Voigt, etc) as well as atmospheric parameters such as temperature and pressure. These parameters help define the interaction between radiation incident on a molecule and the resulting transitions between energy levels (or lack thereof).

This study considered only the HITRAN transmission and emission values for water vapor, which is the main active absorbing gas in the spectral bands considered for this study. This focuses on the impact of moist layers on the IR BTD. HITRAN data was accessed via the HITRAN API (HAPI; Kochanov et al., 2016). We used the water vapor absorption coefficients, with Lorentz broadening, for our wavelength, temperature, and pressure ranges. Lorentz broadening is the combination of natural line broadening and collision broadening (Wang and Modest, 2004). The importance of Lorentz broadening increases with total pressure and, to a lesser degree, decreases with temperature. Since our interest is largely in the lower atmosphere, Lorentz broadening is a more accurate representation than Doppler broadening (which is pressure agnostic and tends to be used in the upper atmosphere). These broadened spectral lines overlap to create the absorption coefficients at certain spectral locations. The tables generated from this are used in Chapter 4.

2.6 Physical basis for the IR BTD simulation

To achieve a good approximation, we can represent the clear-sky nighttime environment in the shortwave to longwave infrared as a non-scattering (conservatively absorbing) regime. This assumption allows us to simplify the derivation of the governing radiative transfer equation (RTE) facilitate development of the FLC simulation (Chapter 4). This method is distinct from the SBDART simulation used to generate Figure 1.3. We chose to develop our own simple radiative transfer simulation in order to gain more precise control over the model.

As mentioned, we ignore scattering in the nighttime radiative transfer. At wavelengths longer than about 3 μm, Rayleigh scattering has a negligible effect on the intensity of radiation (Kopeika et al., 2014), and although solar radiation plays an important role in daytime measurements up to about 4-5 μm, we are considering only nighttime conditions here. This has the advantage of simplifying calculations to gaseous absorption as the only source of extinction, and gaseous emission as the only source of radiation.

The ocean surface is also assumed to be a blackbody for our wavelengths. This simplification is based on a measured average nighttime sea surface emissivity of 0.984 (Konda et al., 1994), where our pure black body emitter has an emissivity of unity. We also assume a plane-parallel atmosphere, which allowed us to ignore the curvature of the Earth. This assumption is reasonable to do because of the relatively thin atmospheric layer of interest, where the planes are nearly flat on a local scale and the bulk of the radiatively active atmosphere being very close to the surface. We thus can compute optical path via the local observer zenith angle.

Lastly, we made the assumption that the simulated satellite was viewing each pixel from the nadir perspective. This is a source of error in the simulation when comparing head-to-head with GOES ABI, as the nadir view represents a shorter geometric (and optical) path length for some pixels when compared to the satellite perspective. This disparity will be stronger at higher satellite zenith angles. The GOES satellites reside over the equator and thus experience the longest path lengths for earth scene pixels closest to the horizons. At these more extreme viewing angles, the nadir assumption in the simulation will cause the water vapor effects to have less impact on the

brightness temperature, reducing the BTD. Since atmospheric water vapor is relatively close to the surface compared to the height of geostationary satellites, this effect is expected to only be a slight underestimation of the FLC effects at higher latitudes.

We derived a version of Schwarzschild's equation (Liou, 2002; Petty, 2006) for the solution to absorption-only radiative transfer to determine the incremental change in spectral intensity (dI_λ), and corresponding brightness temperatures, as a function of changing surface and atmospheric parameters. Invoking the plane-parallel and non-scattering assumptions mentioned above, the extinction (loss) of spectral radiation ($dI_\lambda = -I_\lambda \beta_\lambda^{\text{abs}} ds$) and gain (emission source) of radiation ($dI_\lambda = B_\lambda(T)\beta_\lambda^{\text{abs}} ds$) along an arbitrary path are both dependent on the volume extinction coefficient ($\beta_\lambda^{\text{abs}}$; $\frac{1}{\text{m}}$) and path increment (ds; m). Equation (2.6) shows how the incremental change in spectral intensity depends on the volume extinction coefficient and the blackbody radiance ($B_\lambda(T)$) along the path.

$$dI_\lambda = -I_\lambda \beta_\lambda^{\text{abs}} ds + B_\lambda(T)\beta_\lambda^{\text{abs}} ds \tag{2.6}$$

Since the change in optical thickness ($d\tau_\lambda$) is directly related to the volume extinction coefficient changing with the path ($d\tau_\lambda = -\beta_\lambda^{\text{abs}} ds$), Equation (2.7) is available to describe the change in intensity in terms of the spectral optical thickness, τ_λ:

$$dI_\lambda = I_\lambda d\tau_\lambda - B_\lambda(T) d\tau_\lambda \tag{2.7}$$

Rearranging the terms, we get the differential form of Schwarzschild's equation (2.8):

$$\frac{dI_\lambda}{d\tau_\lambda} = I_\lambda - B_\lambda \tag{2.8}$$

In order to get the expected spectral intensity for Earth's atmosphere system, we must solve Schwarzschild's equation through the atmosphere. Multiplying both sides of (2.8) by $e^{-\tau}$ and applying the chain rule allows us to rewrite the equation as:

$$\frac{d(Ie^{-\tau})}{d\tau} = -Be^{-\tau} \tag{2.9}$$

Integrating (2.9) over the full optical path and rearranging, we can write the equation as (2.10).

$$I(\tau(s_2)) = I(\tau(s_1))e^{-(\tau(s_1)-\tau(s_2))} - \int_{\tau(s_1)}^{\tau(s_2)} Be^{-(\tau'-\tau(s_2))}d\tau' \tag{2.10}$$

The integral solution to Schwarzschild's equation for a satellite residing at the top of the atmosphere (i.e., where $\tau(s_2) \equiv 0$) is specified in Equation (2.11). This requires including the satellite viewing angle (μ) and the respect to the viewing direction flips the sign of the integral. The total optical thickness through the atmosphere is notated with τ^*.

$$I^{\uparrow}(0,\mu) = I(\tau^*,\mu)e^{-\tau^*/\mu} + \int_0^{\tau^*} B^{\uparrow}(\tau')e^{-\tau'/\mu}d\frac{\tau'}{\mu} \tag{2.11}$$

Transmittance ($\mathfrak{T}$) is introduced as the proportion of radiance extincted between two layers. Using $\mathfrak{T}_\lambda^{\uparrow}(\tau_1,\tau_2,\mu) = e^{-(\tau_1-\tau_2)/\mu}$, we can define the expected spectral intensity as (2.12).

$$I_\lambda^{\uparrow}(0,\mu) = \epsilon_{\lambda,sfc}B_\lambda^{\uparrow}(T_{sfc})\mathfrak{T}_\lambda^{\uparrow}(\tau^*,0,\mu) + \int_{\tau^*}^{0} B_\lambda^{\uparrow}(T(\tau'))\frac{d}{d\tau'}(\mathfrak{T}_\lambda^{\uparrow}(\tau',0,\mu))d\tau' \tag{2.12}$$

The change of transmittance with change in optical thickness is known as the weighting function, and can also be cast into height (z) terms. Furthermore, the integral in (2.12) can be discretized, since we will be working within the confines of the GFS model's vertical resolution. Another simplification is the dropping of the surface emissivity term ($\epsilon_{\lambda,sfc} \approx 1$), since we are treating the ocean surface as a blackbody emitter at both wavelengths of interest.

$$I_\lambda^{\uparrow}(\infty,\mu) = B_\lambda^{\uparrow}(T_{\text{sfc}})e^{-\tau_\lambda^*/\mu} + \sum_{i=0}^{N} B_\lambda^{\uparrow}(z_i)\frac{d\mathfrak{T}_\lambda^{\uparrow}(z_i,\infty,\mu)}{dz}\Delta z_i \tag{2.13}$$

From the derived radiance in Equation (2.13), the brightness temperature can be computed using the Planck Function (2.5). Once the brightness temperature has been computed for each

spectral band (11.2 μm and 3.9 μm) a BTD between these two bands can be calculated using Equation (2.14).

$$\text{BTD}_{11.2\mu m-3.9\mu m} = \left(\frac{hc}{k\lambda \ln(1 + \frac{2hc^2}{I^{\uparrow}_{\lambda}\lambda^5})} \right)_{\lambda=11.2\mu m} - \left(\frac{hc}{k\lambda \ln(1 + \frac{2hc^2}{I^{\uparrow}_{\lambda}\lambda^5})} \right)_{\lambda=3.9\mu m} \tag{2.14}$$

To good approximation, this 11.2 μm - 3.9 μm BTD estimate is driven only by water vapor content and temperature (which determine the optical thickness profile of the atmosphere). This physical basis is used in our study to determine when and where the nighttime low cloud test is picking up atmospheric effects instead of low clouds. We also leverage this RTE to conduct simulations of the IR BTD based on model atmospheres (referred to as the FLC simulation). More details on these simulations are given in Chapter 4.

Chapter 3

Case Studies

A main objective of this study was to identify regions which frequently experience non-cloud positive IR BTD, and determine the likely physical cause. Using geostationary imagery, it is feasible for a user to identify FLC signals manually by looking for a distinct border, contiguous shape, and nearby ocean front (Gladkova et al., 2015). When moonlight is sufficient, the DNB is compared to the imagery to help provide evidence that the positive signal is not a true cloud. These cases focus on different local physical scenarios, in which theories are presented on how they could cause the false positive signal.

3.1 Georges Bank, MA, USA

False low cloud signals have been previously identified in Georges Bank region (Miller et al., 2022). These authors postulate that tidal mixing across the shallow bathymetry of Georges Bank and Nantucket Shoals accounts for the observed false cloud phenomenon. However, the authors do not explore the hypothesis in detail. Launching from this seminal work, we begin the case analysis of this research with a deeper-dive study into the physical processes underpinning the Georges Bank region before expanding to other regions.

The Georges Bank and Nantucket Shoals make up two elevated regions of ocean floor near Massachusetts, off of the eastern coast of the United States. The bank region extends over 240 km by 120 km, and is relatively shallow compared to the surrounding Atlantic bathymetry. Figure 3.1 shows the bathymetry of the region. Vertical mixing experienced in Georges Bank is caused by both tidal currents and bottom friction (Yentsch and Garfield, 1981). As the tides come in and out, the moving water is mechanically mixed over the shallow banks, cooling the warmer water at the surface. These well-mixed waters result in relatively cool SST compared to the surrounding waters which are more thermally stratified and relatively warmer near the surface. Whereas the prevailing boundary layer air mass properties (temperature and moisture) are representative of the regional

(relatively warmer SST) conditions, the localized cool SST anomaly can generate a false cloud signal in the IR BTD per the discussion in Chapter 2.

Figure 3.3

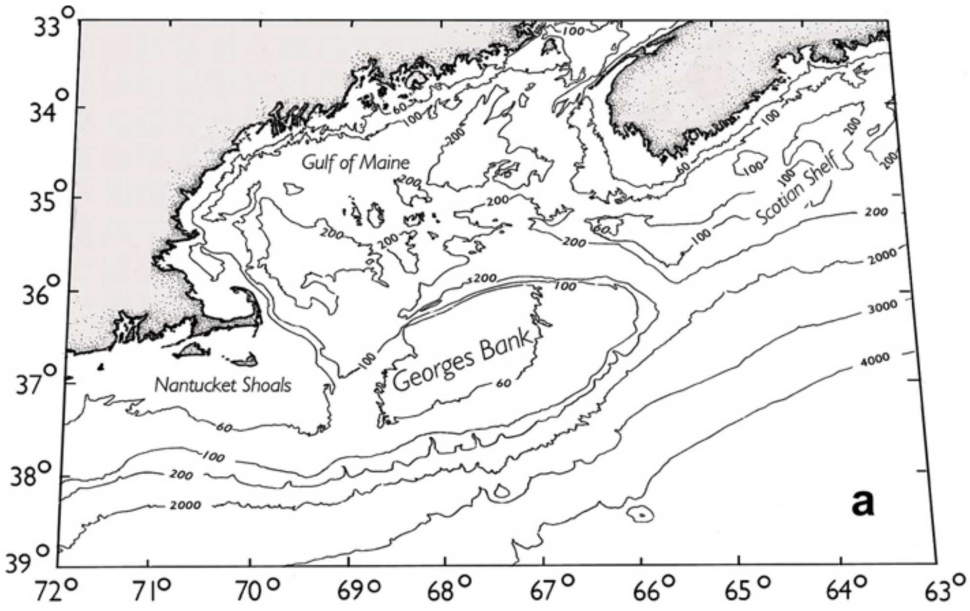

Figure 3.1: Bathymetric map of the Georges Bank and Nantucket Shoals region. Adapted from Steele et al. (2007). Copyright 2007 by Progress in Oceanography, Elsevier.

Figure 3.2 shows the mechanical mixing of caused by an underwater sill, ridge, or bank (representative of the Georges Bank and Nantucket Shoals). As the water fluxes over the restricted vertical region imposed by the underwater bank, it accelerates. The parcel then decelerates on the far side of the bank, causing turbulence. Since water is passed through at each change of the tides, this vertical mixing occurs multiple times per day. The SST discontinuities related to this tidally-induced mixing develops most strongly during the local summer, when the water temperature is maximally stratified (Mavor and Bisagni, 2001; LODER and GREENBERG, 1986). The summer months also correspond to warmer temperatures in general and commensurately higher water vapor content in the lower atmosphere. Juxtaposing these atmospheric conditions with a cool SST anomaly provide the right conditions for the false-alarm scenario considered by Miller et al. (2022) and developed further by this research.

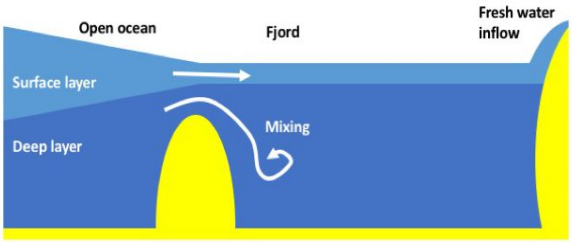

Figure 3.2: Demonstration of tidally-driven cold water upwelling. Adapted from Glessmer (2019), Adventures in Oceanography and Teaching.

Another noteworthy aspect of the process described above, which bears relevance to applications beyond simply identifying areas of potential FLC events, is that upwelling caused by tidal mixing over the bank also mixes nutrients from deeper waters to the surface. This introduction of enhanced nutrients to the near-surface photic zone of the ocean (where sunlight is no yet completely attenuated by water absorption) drives the growth of phytoplankton and zooplankton, which attracts fish to the region (Townsend et al., 2004). Consequently, the Georges Bank region is frequently a productive fishery. When viewed from space, the phytoplankton chlorophyll affects the visual-spectrum color of the ocean, absorbing more blue-spectrum light in the well-mixed regions (Yentsch and Garfield, 1981). This connection between chlorophyll and upwelling regions makes it plausible to estimate upwelling from satellite imagery (Messié and Chavez, 2017). Thus, certain FLC zones that are associated with deep water upwelling may also be identified by way of ocean color signals.

Due to the bathymetry and the tidal mixing effects in Georges Bank and Nantucket Shoals, the discrete cold regions in the SST are seasonally-driven. Figure 3.3 shows monthly SST composites from Yoder et al. (2002). It is very possible that this climatology underestimates the cold SSTs in the Georges Bank region due to the effect of FLCs on the AVHRR-derived SST data record (this is discussed more in Chapter 5. However, the general pattern shows the cold regions over the underwater banks getting relatively colder during the summer months of June, July, and August. This is likely due to the persistence of the tidally-driven vertical mixing. While the rest of the region warms seasonally, the bank regions retain their cold upwelling.

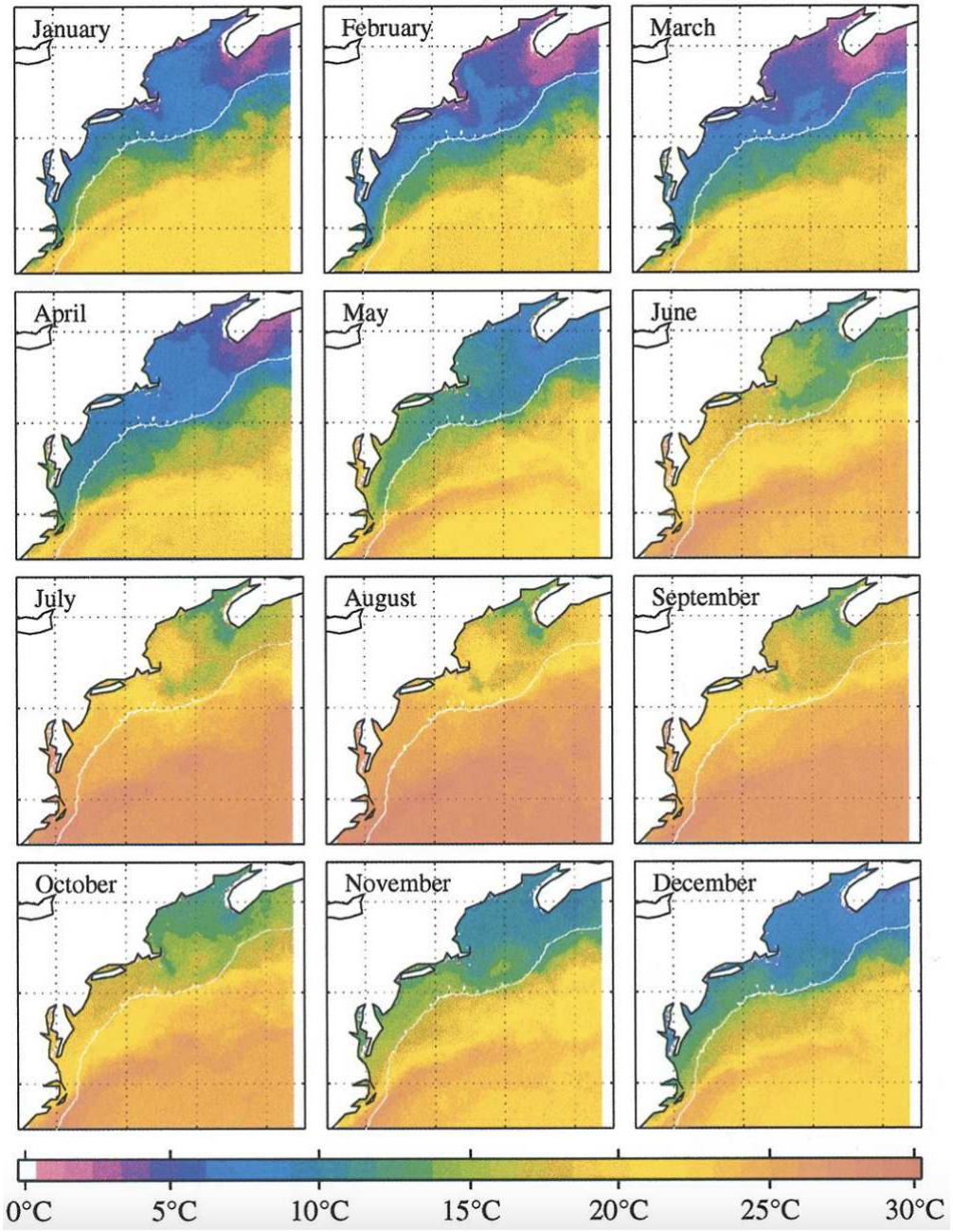

Figure 3.3: SST climatological monthly composites (data from AVHRR SST, September 1997-August 2000). Adapted from Yoder et al. (2002). Copyright 2002 by Wiley, Limnology and Oceanography. Note how Nantucket Shoals and Georges Bank are associated with a distinct cold region in the summer months of June, July, and August.

The first case study of FLCs we considered for this region occurred on the night of 20 June 2024, off the east coast of Massachusetts (Figure 3.4). GOES-16 ABI imagery of this event is shown as the GeoColor product in Figure 3.4b and the IR BTD in Figure 3.4a. Both ABI products show a widespread region of positive BTD along the Maine and Nova Scotia coast. The GOES-16 ABI imagery was captured at 06:00 UTC. NOAA-21 passed over the same region that night at 05:20 UTC. The moon that night was in the waxing gibbous phase, at 98% illumination (https://aa.usno.navy.mil/data/MoonPhases). That amount of illumination makes the VIIRS DNB useful in assessing the presence of clouds over the ocean (Miller et al., 2013). The VIIRS DNB imagery from Figure 3.4c shows far fewer clouds along Georges Bank and Nova Scotia than what is suggested in the ABI imagery (Figure 3.4b and Figure 3.4a).

This discrepancy between the ABI and DNB observing systems provides evidence that the positive BTD in this case was caused by emission from the water vapor instead of true low cloud coverage. In order to check this hypothesis, Figure 3.4d shows the radiosonde sounding launched at 00:00 UTC from Yarmouth, Nova Scotia, earlier in the day before the satellite observations. The sounding shows both an increase in humidity and temperature (a low-level moist inversion) around 950 hPa. Although almost six hours before the satellite imagery, there was a warm and moist air mass present. Given the known connection between warm and moist air masses and FLCs, and the discrepancy between ABI BTD and VIIRS DNB, it is likely that much of this measurement is FLC.

Figure 3.5 shows another case study for the Georges Bank region, this time on 17 September 2024. The IR BTD from 00:00 UTC (Figure 3.5a) and 06:00 UTC (Figure 3.5b) shows a large region of positive measurement, which would often be associated with low cloud coverage. However, a supermoon (full moon coinciding with perigee) was present that night, and allowed the DNB imagery in Figure 3.5c to clearly resolve the cloud coverage. The large swath of IR BTD measurements at about +1 K do not appear in the visible-spectrum DNB image. In addition, this region of positive IR BTD does not evolve much between 00:00 UTC and 06:00 UTC, lending further evidence that this is FLC. A radiosonde launched from Yarmouth Airport (YQI) confirms

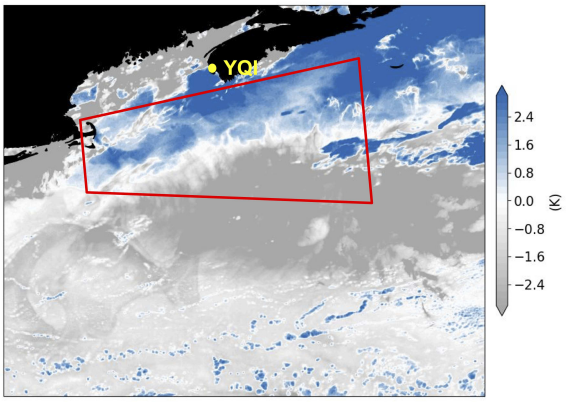

(a) 11.2 µm - 3.9 µm BTD: 2024-06-20 05:20 UTC

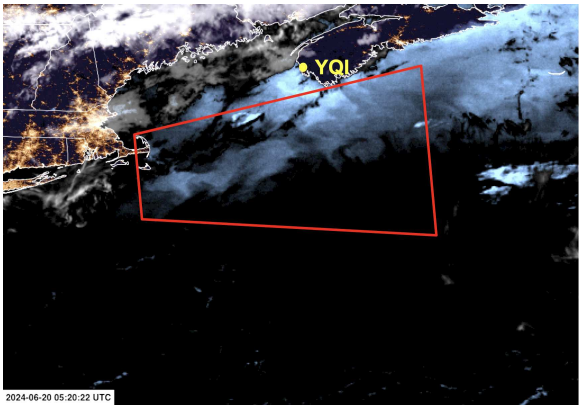

(b) GeoColor: 2024-06-20 05:20 UTC

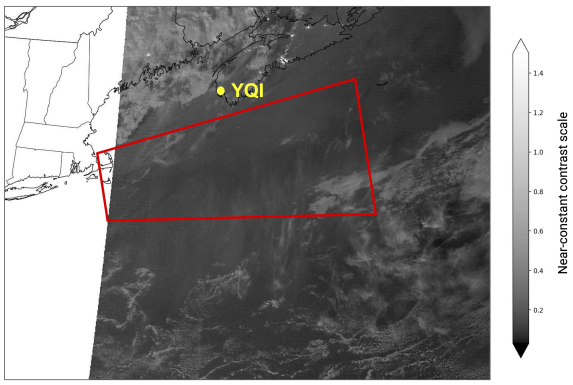

(c) VIIRS DNB (NOAA-21): 2024-06-20 05:20 UTC

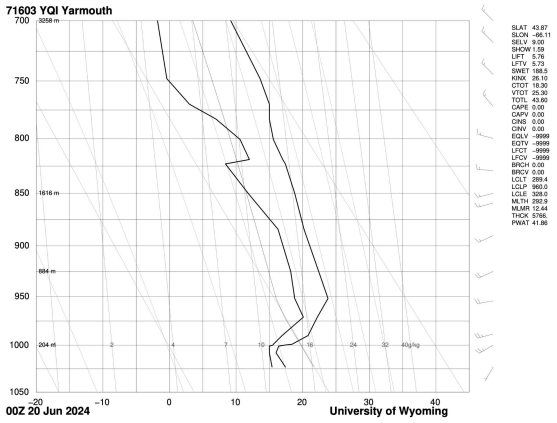

(d) YQI Atmospheric Sounding: 2024-06-20 00:00 UTC

Figure 3.4: (a) The 11.2 µm - 3.9 µm brightness-temperature difference is positive along the range in blue. The region of suspicious low cloud signals are outlined in red. (b) GeoColor imagery from GOES-16 ABI shows maritime low cloud coverage along the east coast of the US and Nova Scotia. (c) The NOAA-21 VIIRS Day/Night Band was employed to determine whether this signal was due to low clouds, or a moist and warm air mass over cold waters (false low cloud). On a night with 98% moon illumination, much of the area near the low-cloud signal does not show clouds in the Day/Night Band visible imagery. (d) Five hours before the satellite observations, a radiosonde was launched from Yarmouth Airport (YQI). This atmospheric sounding observed a moist inversion. This correlation provides further evidence that a moist and warm air mass may have caused the positive 11.2 µm - 3.9 µm brightness-temperature difference, instead of actual low clouds present in the region.

a low-level inversion near the region. However, it does not necessarily confirm moisture in the low atmosphere, necessary for the generation of FLC signals. Despite this, it is likely that much of this IR BTD measurement is FLC.

In previous studies, features in the nighttime low cloud field are initially investigated due to suspicious shapes and longevity in geostationary satellite imagery (Miller et al., 2022; Gladkova et al., 2015). Some of these cloud signals are confirmed as FLCs near Georges Bank by using the VIIRS DNB and CALIPSO lidar to show the presence of clear sky in the region (Miller et al., 2022). The offending signals are often described as stationary outlier features, or like background noise. Since FLCs are locked to the region of suppressed SST, they drift and evolve at timescales much slower than the meteorological cloud field. Thus, these features appear static compared to the clouds, often retaining a specific shape over an entire night, or a slowly evolving shape over multiple nights.

By leveraging the temporal resolution of GOES-R ABI, we can highlight these stationary 'cloud' signals by taking a long-term average of the IR BTD. Figure 3.6a shows a positive BTD at 06:00 UTC on 1 July 2023. Figure 3.6b shows a time-lapse generated by collecting one image from each night (at 06:00 UTC), filtering the images to only positive BTD, then averaging the images together. The longer time-frame allows transient cloud features to blur and constant cloud features to sharpen in the foreground. By the end of July 2023, the average positive IR BTD congregates around Georges Bank and Nantucket Shoals. These static positive BTD signals are locked to the cooler SSTs caused by the upwelling from the shoals in this region.

In order to test the hypothesis that these positive IR BTD signals are due to coupled water temperature and air mass effects and not due to low clouds, the composite average imagery was extended to each month of the year. Figure 3.7 shows how the low cloud measurements tend to congregate around the Nantucket Shoals and Georges Bank bathymetry features in the summer. In the winter, the IR BTD shows a dispersed and varied signal. The strength of the bathymetry-driven FLC signal appears to be dependent on the season, with a pronounced tendency toward the warmer months of June, July, and August. This pattern mirrors the SST climatology shown in

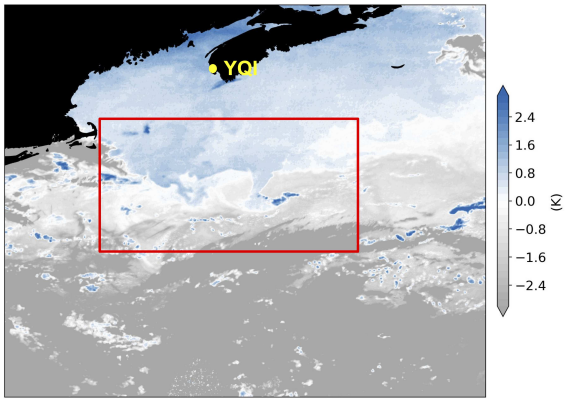

(a) 11.2 µm - 3.9 µm BTD: 2024-09-17 00:00 UTC

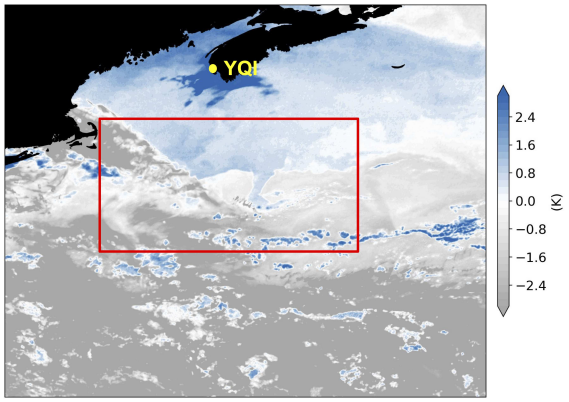

(b) 11.2 µm - 3.9 µm BTD: 2024-09-17 06:00 UTC

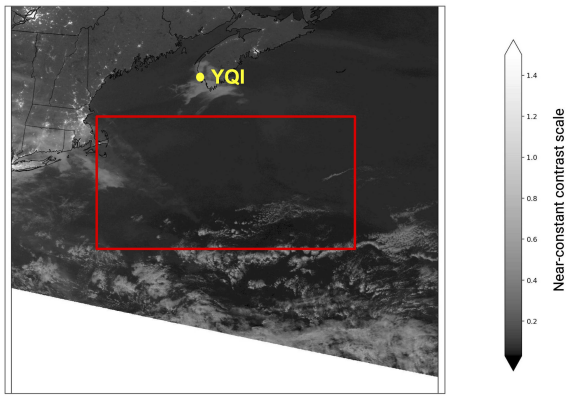

(c) VIIRS DNB (NOAA-21): 2024-09-17 05:50 UTC

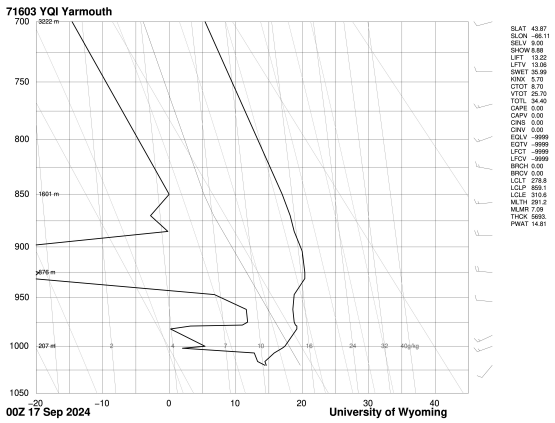

(d) YQI Atmospheric Sounding: 2024-09-17 00:00 UTC

Figure 3.5: (a) and (b) The 11.2 µm - 3.9 µm brightness-temperature difference shows extensive positive along the northern half of the image. Note how the high clouds (gray) evolve over the time difference, but the low clouds (blue) stay relatively similar. (c) The NOAA-21 VIIRS Day/Night Band shows some clouds on the southern coast of Nova Scotia and near Rhode Island, but clear sky over much of the ocean showing positive IR BTD in (a) and (b). 17 Sep 2024 was the night of a supermoon, providing more than enough visible-spectrum light for the DNB to resolve clouds. (d) Radiosonde launched from Yarmouth Airport at 00:00 UTC. This atmospheric sounding observed a low-level inversion. The presence of moisture, which is necessary to observe FLCs, is not as clear from the sounding. Given the evidence from these components, it is likely that much of the positive extent in the IR BTD is FLC.

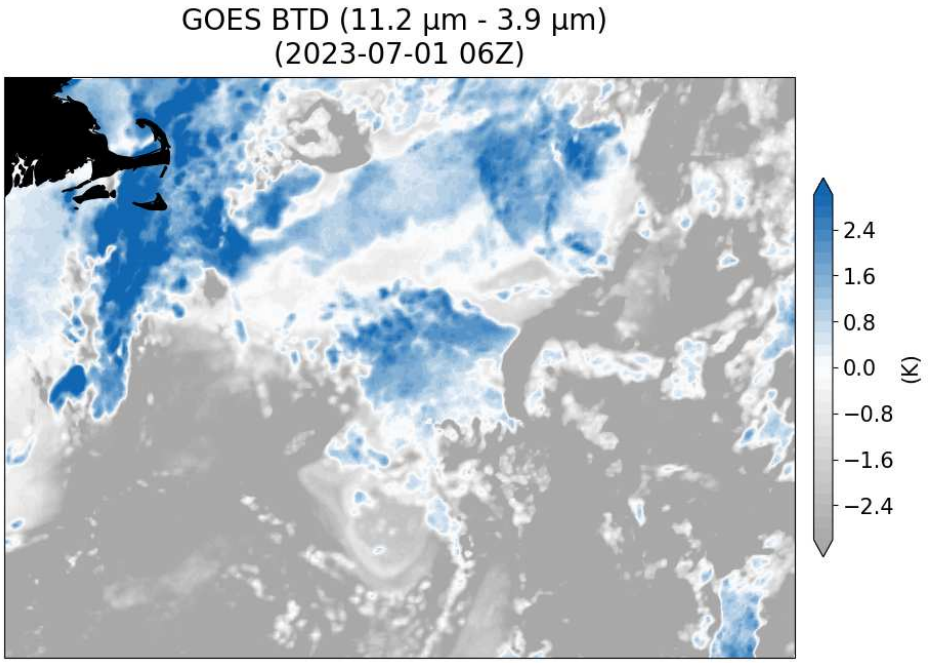

(a) One day of brightness-temperature difference

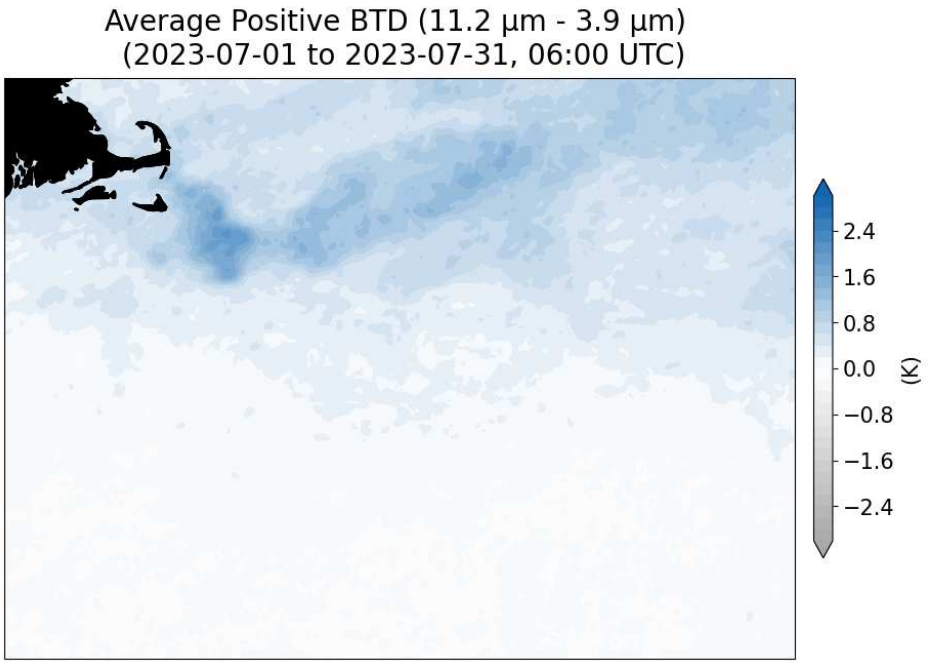

(b) Full month of brightness-temperature difference

Figure 3.6: (a) shows a snapshot of the 11 µm - 3.9 µm positive IR BTD, showing both real and artificial low cloud signals. (b) shows longer-term analysis generated by averaging the positive IR BTD of each night at 06:00 UTC to pull out the stationary signals. These stationary signals are likely to be caused by consistent cold pools in the SST, which produce positive IR BTD signals when there is moist, warm air aloft.

Figure 3.3. This finding suggests that sufficient warm air above the localized SST cold pools may contribute to generating the positive signals in IR BTDs. In this case, the cold upwelling is locked to the underwater banks, so when the air is more frequently warm and moist, the same FLC shape appears repetitively.

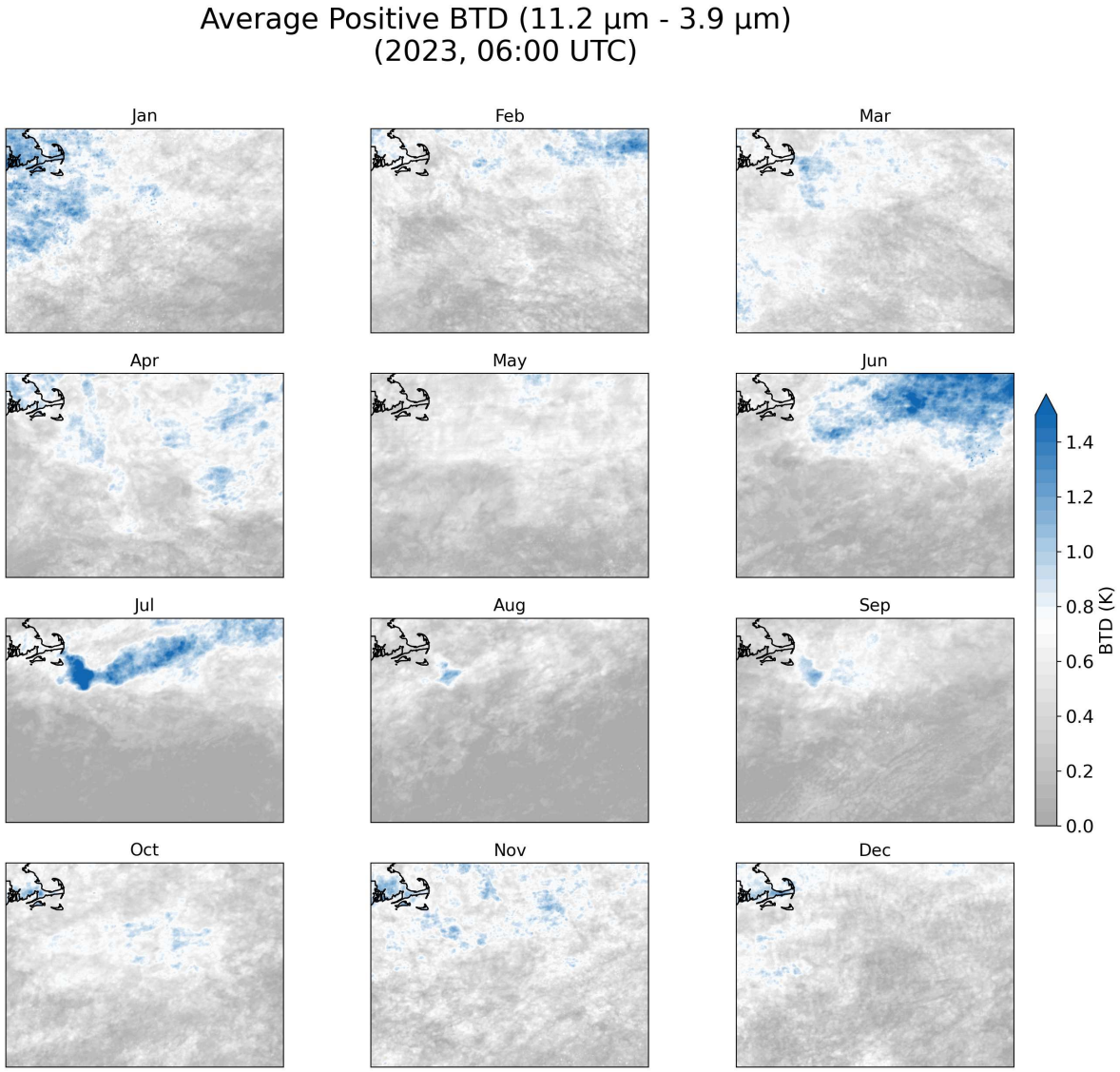

Figure 3.7: The composite 11.2 µm - 3.9 µm positive IR BTD from GOES-16 ABI for each month in 2023. The IR BTD was measured each day at 06:00 UTC (nighttime in the region), and averaged over the time series to create the composite. Note how the false low cloud features appear in the summer, peaking in July.

The Georges Bank and Nantucket Shoals region frequently experiences FLCs in the nighttime IR difference due to the sharp SST gradient caused by tidal mixing over undersea plateaus. During the summer, when moist warm air masses are common, this frequently creates the moist inversion. Other regions that have similar upwelling are more likely to also have FLC effects at night when the local atmosphere is warm. This includes the four major upwelling systems: California, Peru, Northwest Africa, and Benguela (Messié and Chavez, 2017). The California coast has been known to be associated with FLCs at night (Miller et al., 2022). However, upwelling over undersea banks is only one method of creating a strong SST gradient. Next, we will use a case study to discuss wind-driven upwelling.

3.2 Southern Coast of Oaxaca, Mexico

The southern coast of Oaxaca, Mexico is characterized by strong mountain-gap wind known as the "Tehuantepecer" (Romero-Centeno et al., 2003). Tehuantepec itself is an isthmus between the Gulf of Mexico and the Pacific ocean. The 40 km gap in the Sierra Madre mountain range accelerates the wind from north to south into the Gulf of Tehuantepec ($\sim$16° N, 95° W). These winds can cause a significant drop in the SST in the region immediately south of the bay (Stumpf, 1975). This cooling effect is due to mechanical mixing, where the offshore (northerly) winds impart momentum on the ocean surface and push the warmer surface waters away. These waters are replaced by the upwelling of colder water from below and entrainment of water from the sides. This process results in an isolated region of relatively cooler SSTs in the mixing zone.

Romero-Centeno et al. (2003) shows that the Tehuantepecer winds have a strong seasonal signal, with maximum values during December and January. This seasonality is due to the pressure differences across the isthmus that occur during the winter months. Given its tropical location, warm and moist maritime air dominates the region, creating a potential environmental set-up for FLCs.

During February 2023, the Gulf of Tehuantepec experienced periods of strong northerly wind interspersed with periods of relative calm. These "on/off" conditions provided an opportunity to assess possible correlations between positive IR BTD and periods of strong Tehuantepecer winds.

On 19 February 2023, strong Tehuantepecer winds of about 20 m/s were shown in the GFS model. On this day, the OISST product revealed a regionally-confined cold pool (of depressed SST), with SSTs dipping to values of 294 K. The surrounding SSTs were warmer, generally greater than 299 K. Inspection of GOES ABI imagery revealed a positive IR BTD in the region corresponding to this localized SST cold pool (Figure 3.8).

In comparison, on 22 February 2023, the Tehuantepecer winds had calmed to near 0 m/s in the region. The OISST retrievals show significantly warmer SSTs, only reaching low temperatures of approximately 298 K. The IR BTD did not show positive values for this case, consistent with the lack of required ingredients for FLC signals caused by warm and moist air over relatively cold SSTs.

Another cold SST anomaly feature further southeast from the Gulf of Tehuantepec is created by the Papagayo jet (Chelton et al., 2000). Similar to the Tehuantepecer winds, the Papagayo winds are accelerated by a narrow mountain pass, and cause downstream cold-water upwelling. Also like the Tehuantepecer, the strongest winds occur in winter, when the air temperature gradient across the isthmus is largest. The two wind-blown regions appear in satellite data and retrievals both in terms of SST suppression and chlorophyll-a enhancements. In our case study, the Papagayo jet is present on both 19 February and 22, and appears to be associated with positive IR BTD. Also similar to the Tehuantepecer, the stronger Papagayo jet winds of $\sim$15 m/s on 19 February is associated with SSTs of $\sim$293 K and an IR BTD of $\sim$2 K. The weaker Papagayo jet winds of $\sim$10 m/s on 22 February are associated with a warmer local region of $\sim$295 K and an IR BTD of $\sim$0 K.

In this way, revealing the underlying physical processes helps us to anticipate other parts of the world where we might expect to find similar artifacts in the satellite-derived products, as well as regions predisposed to maritime advection fog formation. Similar mountain-gap flow winds toward the ocean occur in other regions of the world.

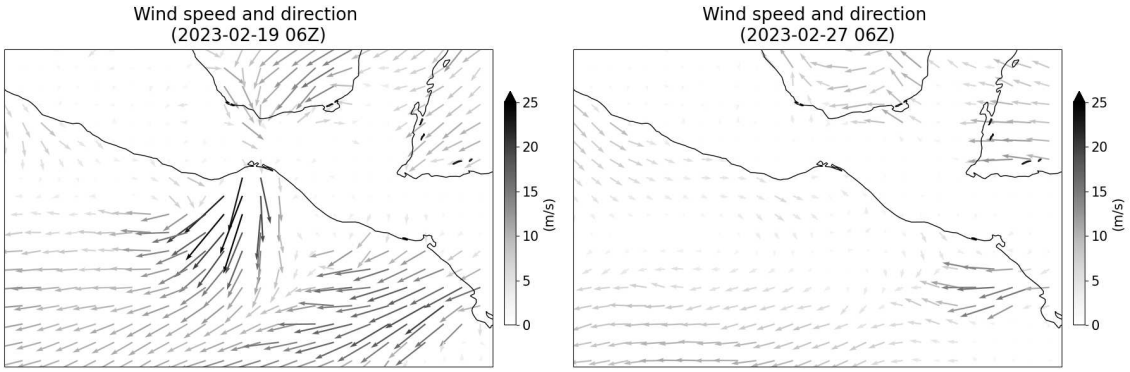

(a) Tehuantepecer winds from GFS model

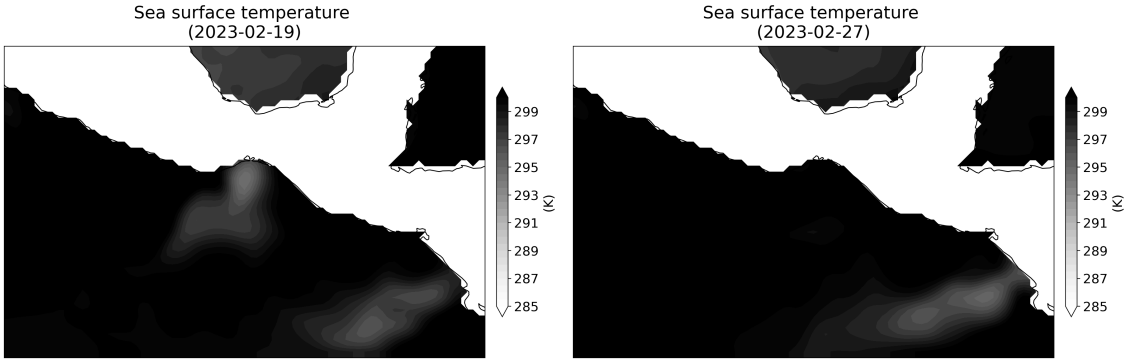

(b) NOAA optimum interpolation sea-surface temperature

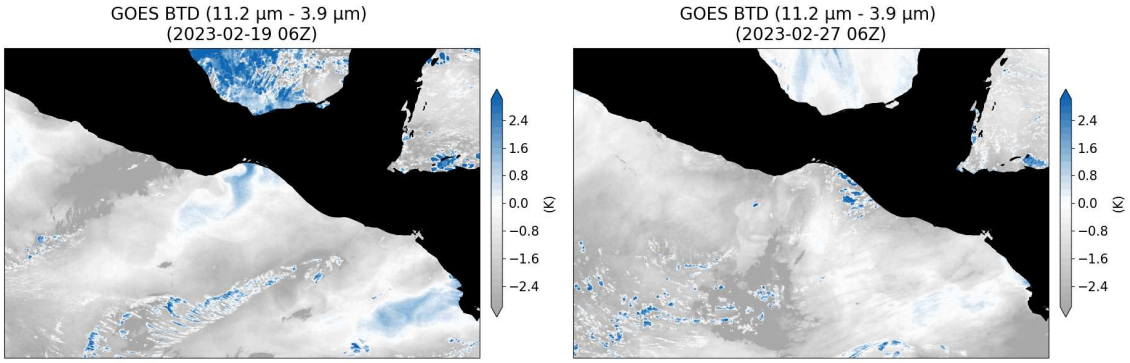

(c) GOES LWIR-SWIR brightness-temperature difference

Figure 3.8: Comparisons between GFS model-analyzed 2-m winds (a), satellite-derived SST (b), and satellite-observed IR BTD (c) for a region of Central America where gap wind flows occur. The left-panel images show conditions when these gap flows are strong, and the right-panel images show conditions devoid of gap flows. In the left-panels, cold pools of SST (b) are created by strong Tehuantepecer and Papagayo jet winds, resulting in positive 11.2 μm - 3.9 μm BTD signals (c) in the bay to the south. The right images show that, when these gap-flow winds are not present, neither the cold pool nor the positive BTD are produced.

For example, the Strait of Gibraltar, a narrow water passage between southern Spain and north-western Africa and connecting the Atlantic Ocean with the Mediterranean Sea, experiences similar wind-driven upwelling which results in its own cold pool (Stanichny et al., 2005). Figure 3.9 shows an example of wind-driven cold upwelling, from 27 July 2003 to 17 August 2003. When warm and moist air is available, similar false clouds effects will likely be seen in the IR BTD.

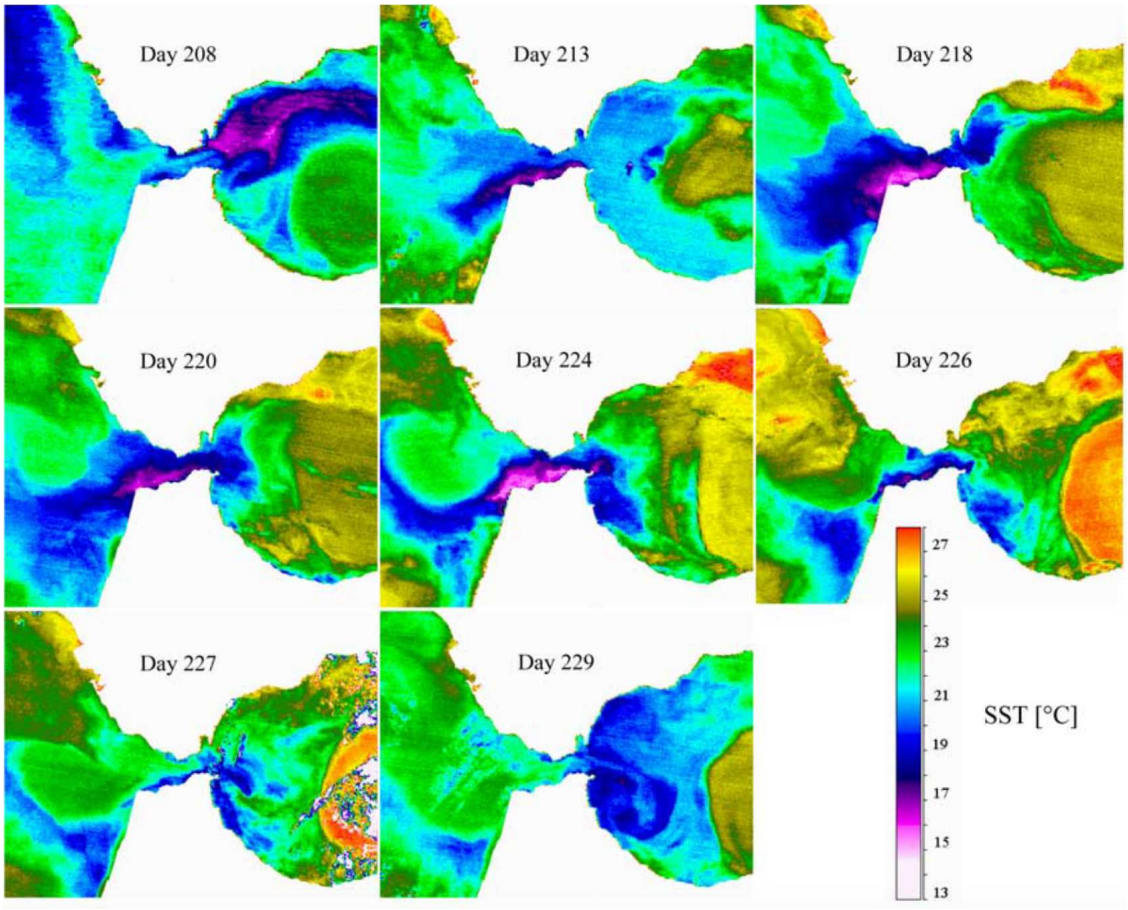

Figure 3.9: Wind-driven upwelling in the Strait of Gibraltar corresponding to the westward prevailing winds during days 208–229 of year 2003. MODIS SST maps show the development and localization of the cold region (7°W–4°W, 35°N–37°N area). Adapted from Stanichny et al. (2005). Copyright 2005 by Geophysical Research Letters, American Geophysical Union.

The Strait of Juan de Fuca in the Northwest US (Washington State) is another example of gap winds accelerating toward the ocean. This region is important to military interests, and includes a number of US Navy facilities, including Whidbey Island Naval Air Station, the Bangor Submarine

Base, the Everett Homeport, and the Bremerton docks (Navy Mesoscale Primer: Gap Winds; https://www.atmos.washington.edu/~cliff/Navygap5.html). The gap winds in the Strait of Juan de Fuca can generate winds at speeds of 13-15 m/s when a high-pressure region exists over Canada and a low-pressure region exists off the Washington State coast (Overland and Walter, 1981). These high winds can create a feature in the Pacific Ocean known as the Juan de Fuca Eddy, an isolated tongue of well-mixed cold water (Klymak et al., 2023). The Eddy could also fit with the discussion in Section 3.1 because the vertical mixing is associated with a region where the shelf widens abruptly in the lee of a bank. The separation that defines this cold region is visible in both satellite-derived SST and chlorophyll measurements.

The cases of non-cloud positive IR BTD in Southern Oaxaca associated with gap wind upwelling lend further evidence for the ulterior cause of the positive BTD signal by cold sea surface and warm, moist air masses. Similarly to the Georges Bank region, Southern Oaxaca experiences a seasonality to its FLC signals. Unlike the Georges Bank region, these cold pools are not rooted to a static bank below the water, and are instead determined by the strength of the Tehuantepecer wind.

Underwater banks and gap flows are two methods of cold water upwelling. Another source of relatively cold SST regions are cold core eddies that can occur on the interface of strong currents. This will be discussed next, in Section 3.3. All of these physical phenomena represent regions that may be more likely to experience FLC effects when warm and moist air is present.

3.3 The Gulf Stream and US East Coast

The Gulf Stream is characterized by warm water traversing from south to north along the east coast of the United States and Canada (Richardson, 2001). It originates in the Gulf of Mexico, moves northward along the eastern seaboard, then turns northeastward, continuing toward northwest Europe. It exists alongside the Labrador current, which brings cold water southward from the Arctic along the poleward side of the Gulf Stream. The juxtaposition of the two water masses creates a scenario where warm and moist air associated with the warm water can transport over

the cold water—presenting the conditions necessary for FLC signals. The Gulf Stream region is known to frequently have FLC signals (Gladkova et al., 2015).

In the previous case studies, isolated regions of cold water were shown to originate from upwelling processes. Mechanically, the Georges Bank region experiences upwelling from the topography of the ocean floor, whereas in the Southern Oaxaca region gap-flow winds advect away the surface warm water, causing cold upwelling from beneath. Yet another source of SST gradient is the synoptic scale poleward transport of warmer mid-latitude and tropical waters, where they interface and mix with the cooler waters of these high-latitude regions. In this section, we investigate the effects of large-scale ocean currents on the IR BTD, focusing on the Gulf Stream in the northwest Atlantic.

The Gulf Stream is inherently unstable due to the stark differences in temperature and salinity between it and the Western Atlantic (Schultz, 2015). These dynamics cause the Gulf Stream's distinctive meandering path, and the large rotating eddies that break off 5-8 times a year. These eddies are 50 to 150 km wide, and can be cold- or warm-core.

For the Gulf Stream region, the transport of warm moist air over cold water is generally associated with winds from south to north or southeast to northwest. June 2024 experienced both southerly and northerly winds. Figure 3.11 compares the IR BTD for different wind directions. The period of more southerly wind shows swirling features at about +1 K in the IR BTD. When the wind is more northerly, these eddy features are not visible.

Figure 3.10 shows an example of a Gulf Stream eddy (circled in red) being visible in the IR BTD from GOES-16 ABI for one environment and not the other, despite consistently existing the SST. The eddy is visible in the IR BTD on 17 Apr 2023, when the wind is southwesterly, likely bringing warm moisture in the atmosphere. On 27 Apr 2023, the wind is northeasterly and likely bringing cooler and drier air over the eddy region. This results in the disappearance of the feature from the IR BTD.

Figure 3.11 shows another example, this time with more broad swirling features. The swirling features in the positive IR BTD on 9 Jun 2024 (Figure 3.11b) match the SST contrast pattern that

exists in the SST of the Gulf Stream. Comparing this to 29 Jun 2024 (Figure 3.11a), when the wind is generally more northerly (or calm), we find that these swirling SST features are no longer visible in the IR BTD. Overriding clouds are present on 29 Jun 2024, muddling the imagery, but the southern half shows none of the swirling features from 9 Jun 2024. The SST data shows that the meandering intersection of cold and warm SST remained present for both dates.

These comparisons offer prime examples of the positive signal being locked to the shape of the SST cold pool and also tied directly to the nature of the overriding air mass. Importantly, both these comparisons were conducted during the same month, such that both involve similar SST conditions and eddy dynamics. The delineating conditions which determine visibility of the IR BTD are tied directly to the wind direction, which demarcates a cooler and drier continental air mass (northerly winds coming off the North American continent) and warmer and moist maritime air mass (southerly winds from the lower latitudes of the tropical Atlantic and Gulf of Mexico).

It is unlikely that cloud physics alone would generate a shape with edges as distinct as the Gulf Stream eddy or swirling features; even if advection fog were to form, the prevailing winds would drift these features downstream from the formation region, which is not evident in the geostationary satellite imagery sequences analyzed for this region. For currents that generate cold-core eddies such as these, looking for these ocean temperature features in the IR BTD can help to determine if a positive signal is low cloud or a warm and humid air mass over a cold pool. Eddy features in the IR BTD are also frequently seen near the Kuroshio Current of the Pacific Ocean (Gladkova et al., 2015), suggesting yet another potential regional source for low cloud false alarms and associated SST climatological warm biases.

Products such as the ACSPO, the NOAA Enterprise SST system, rely on versions of the IR BTD to mask out clouds. FLC signals can cause masking in these regions where the moist inversion recreates the positive BTD. Cloud masking that follows the pattern of a sharp SST gradient, such as in Figure 3.12, is often the result of FLC errors. The visualization for Figure 3.12 is from CIRA's web-based image looping tool SLIDER (https://rammb-slider.cira.colostate.edu), using data from GOES-16 (East; 75.2W). Blue on the color bar is 15° C and red is 30° C.

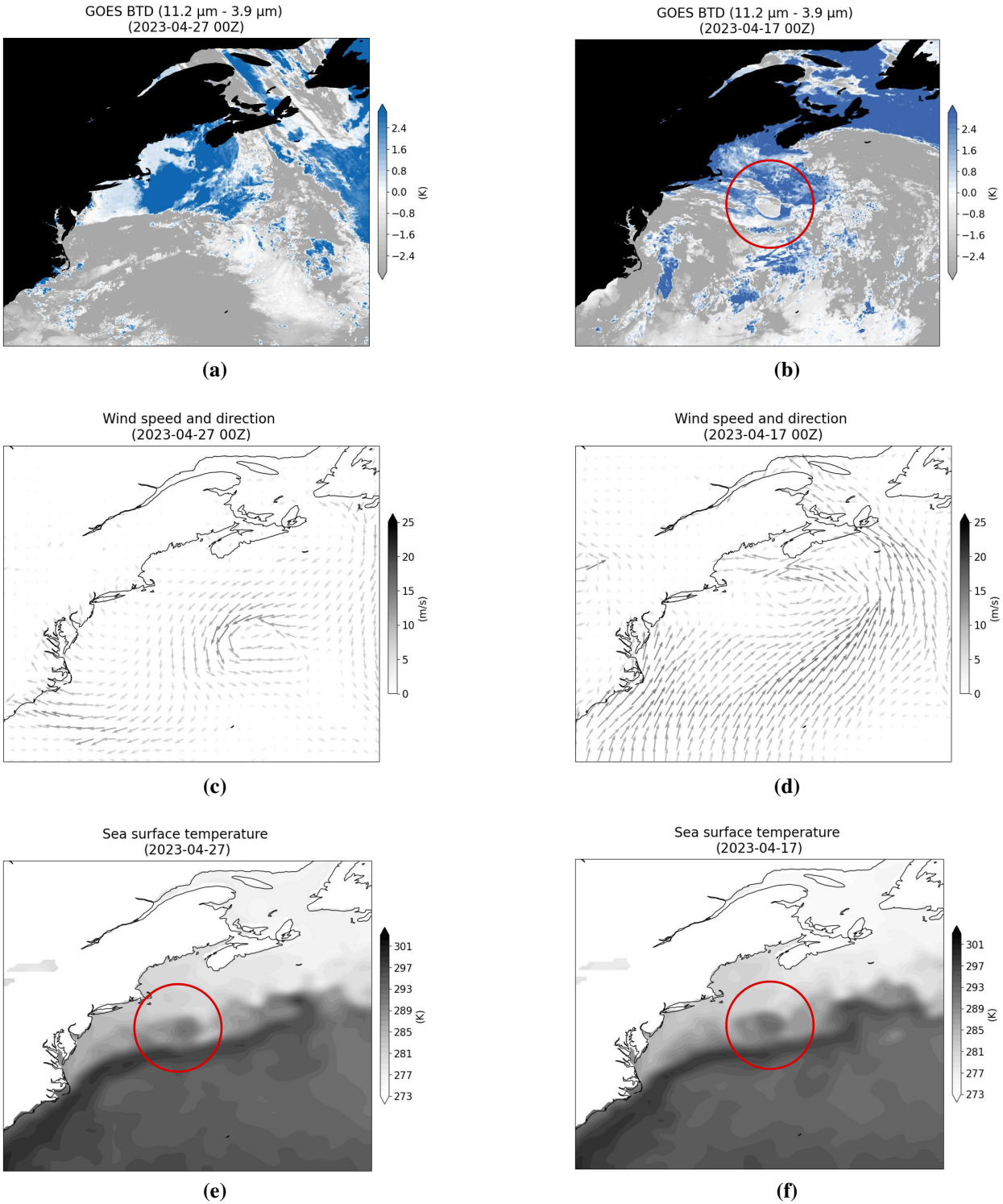

Figure 3.10: (a), (c), (e): On 27 Apr 2023, no circular eddy feature appears in the 11.2 µm - 3.9 µm BTD, despite its presence in the SST (circled in red). The wind is northeasterly, and is likely advecting cooler, drier air. (b), (d), (f): On 17 Apr 2023, a Gulf Stream eddy is visible in the 11.2 µm - 3.9 µm BTD (circled in red). The southwesterly wind is likely transporting moist and warm air over the cold water, resulting in false low cloud signals locked to that SST feature.

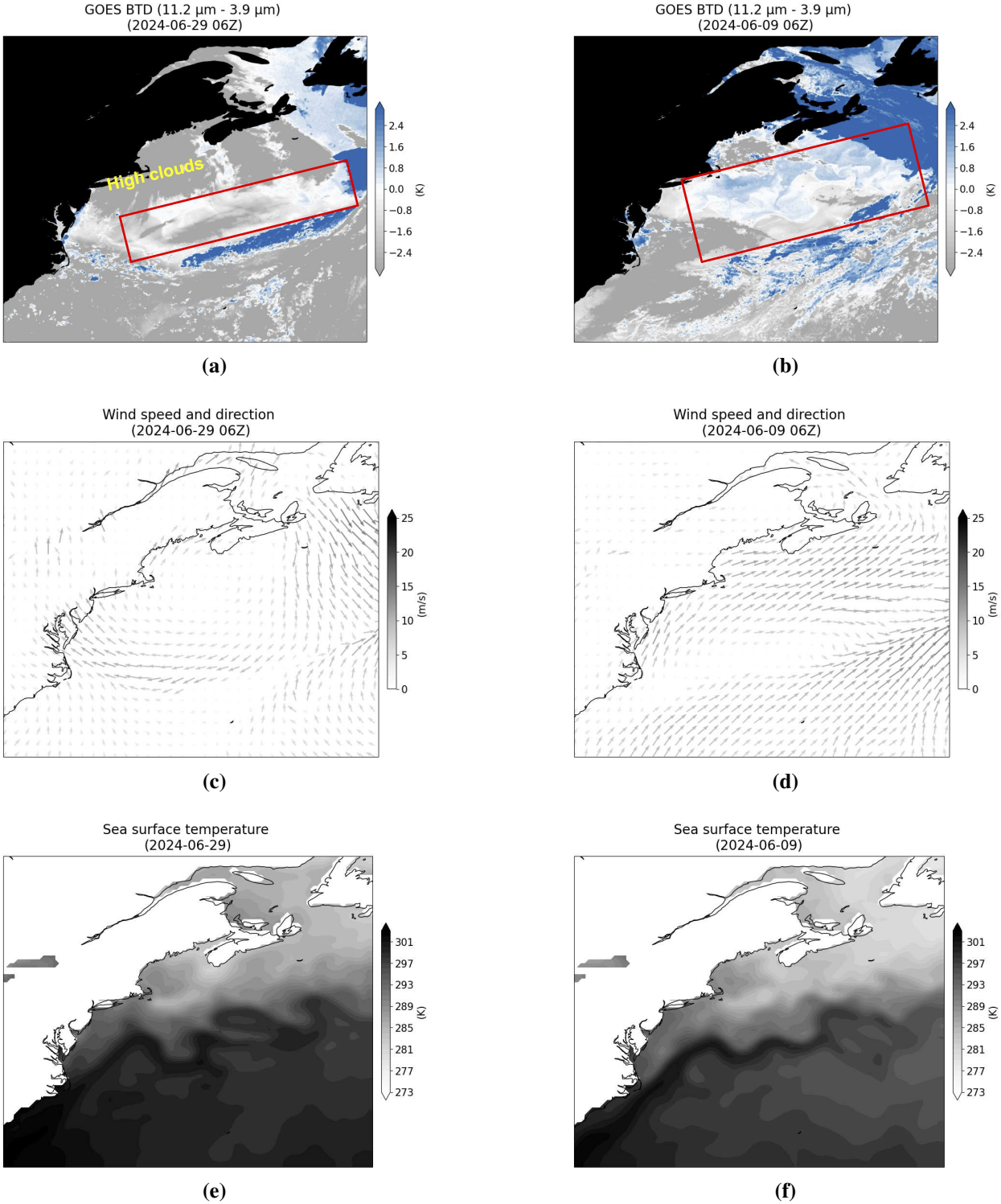

Figure 3.11: (a), (c), (e): On 29 Jun 2024, a northeasterly wind in the Gulf Stream results in no visible SST features in the 11.2 µm - 3.9 µm BTD, likely because of the cool and dry incoming air mass. (b), (d), (f): On 9 Jun 2024, SST features are visible in the 11.2 µm - 3.9 µm BTD at about 1 K. The southwesterly wind is likely transporting moist and warm air over the cold water, resulting in false low cloud signals.

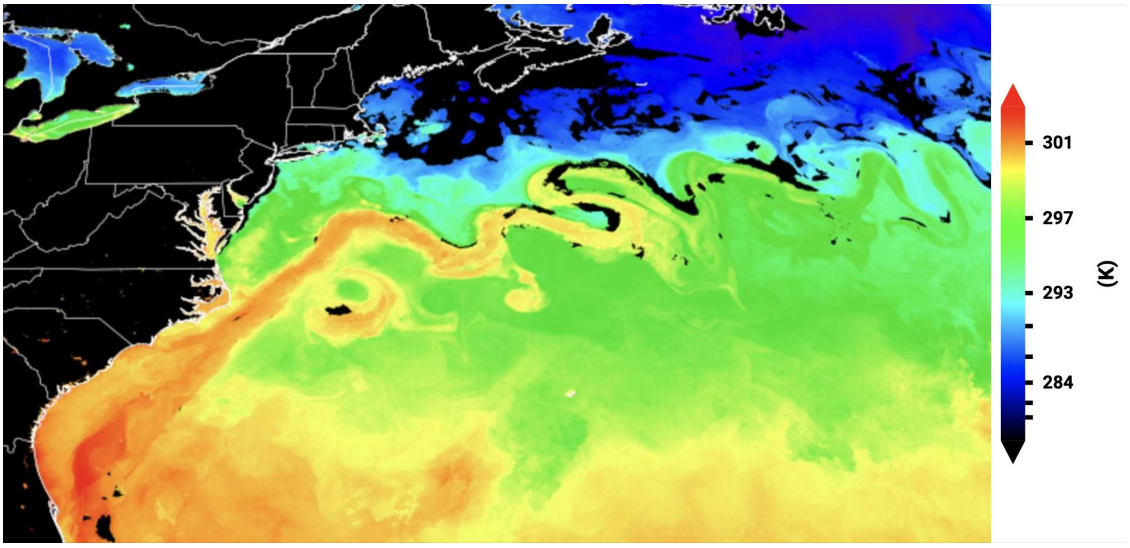

Figure 3.12: Advanced Clear Sky Processor for Ocean (ACSPO) SST product from 25 Jun 2024 at 15:00 UTC. The product shows cloud masking (black) at the intersection of cold and warm waters. This is where the warm and moist air masses are likely causing a false cloud signal in the IR BTD.

In 8 July 2024, Hurricane Beryl made landfall in the Gulf Coast of the United States. Over the following six days, the moist air mass from the deteriorating storm flowed over the Gulf Stream region. Figure 3.13 shows how the arrival of the moisture dramatically increased the positive extent in the IR BTD. 11 July 2024 is before the moisture arrives, and 12 July 2024 is while the moist air mass is over the Gulf Stream. 14 July 2024 shows the moist air mass continuing to move toward the east. The cold SST regions become "highlighted" by positive IR BTD, suggesting that these are FLC signals. Note the similarity between the shapes of the positive IR BTD and the SST for 13 July, when the moisture was most directly over the cold side of the Gulf Stream.

Figure 3.14 compares the pattern of low cloud measurements (from the IR BTD) during the summer and winter near the Gulf Stream. During the summer, more frequent FLC events on the cold side of the Gulf Stream have driven the average IR BTD to only be positive on that side. The Georges Bank signal is also visible in the July average, as discussed in Chapter 3.1. During the winter, the low cloud signals are much more evenly dispersed. This may be due to the lack of warm air masses in the winter, which relieves it of the FLC events that occur during the summer. Since the eddy pattern in the Gulf Stream SST is not static on the time scale of a month, any eddy features have been blurred out in the average.

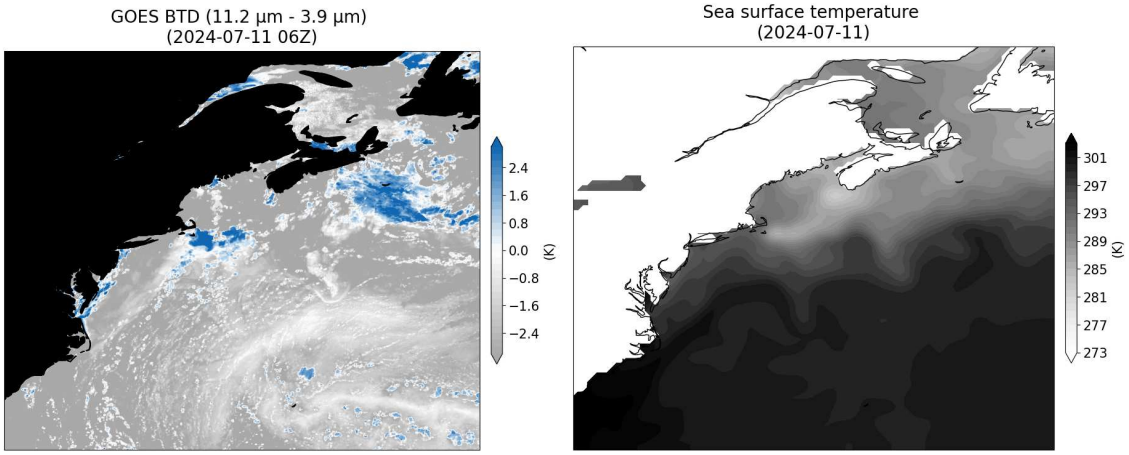

(a) Prior to arrival of moist air mass from Southwest

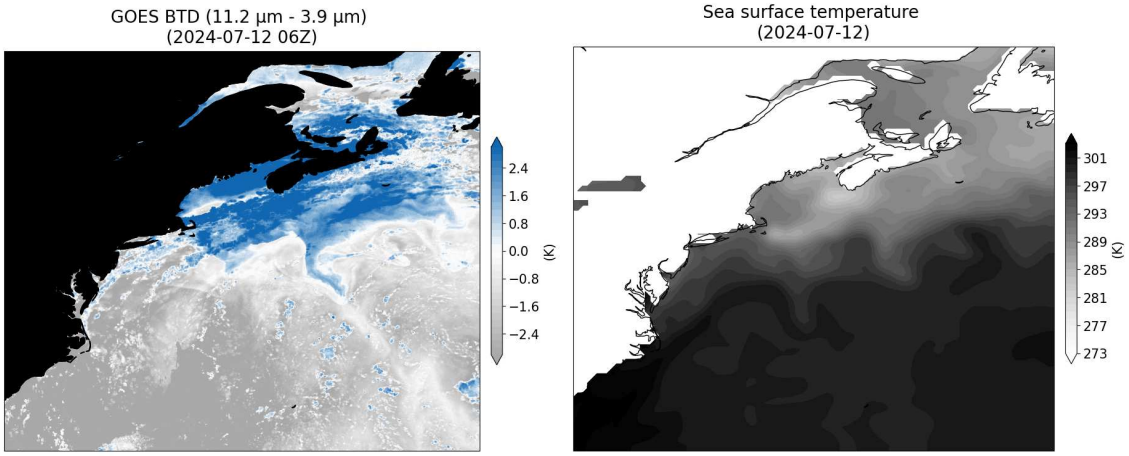

(b) Moist air mass overhead the Gulf Stream region

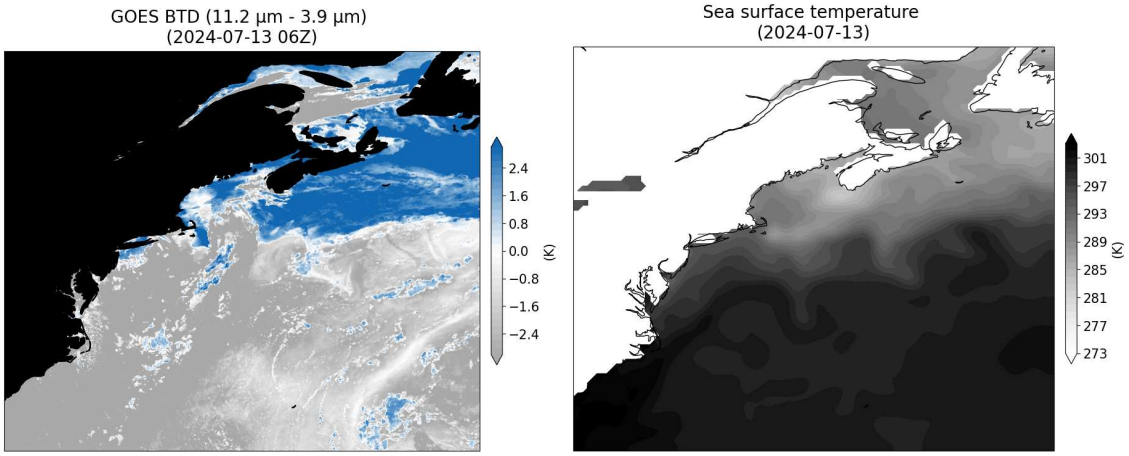

(c) Post moist air mass, it is now mostly to the east of the region

Figure 3.13: The remnants of Hurricane Beryl caused a large moist air mass to arrive over the Gulf Stream on 12 July 2024. The moisture caused a large extent of positive 11.2 µm - 3.9 µm BTD to appear over the cold region of the SST. Note how the shape of the positive BTD matches the underlying cold SST on 12 Jul 2024 (b). This is an example of how moisture transport can cause the appearance of false low cloud signals.

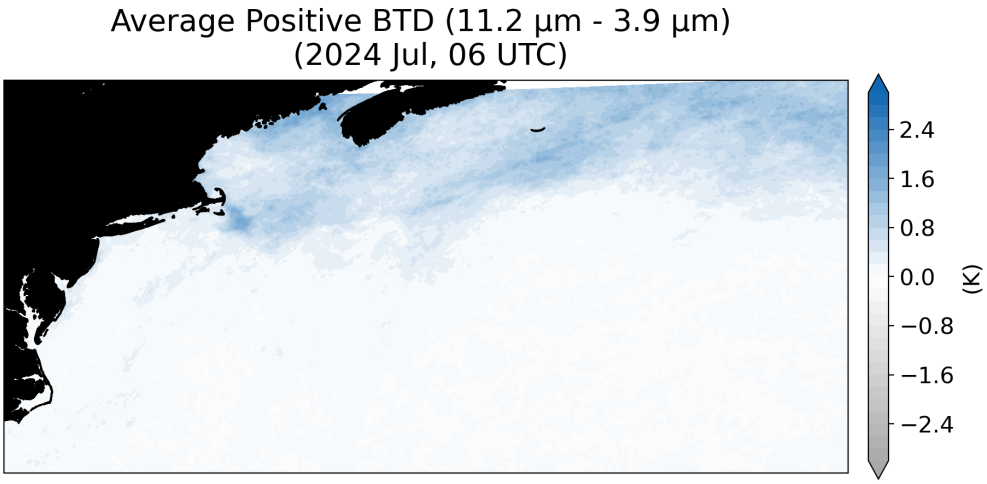

(a) Summer

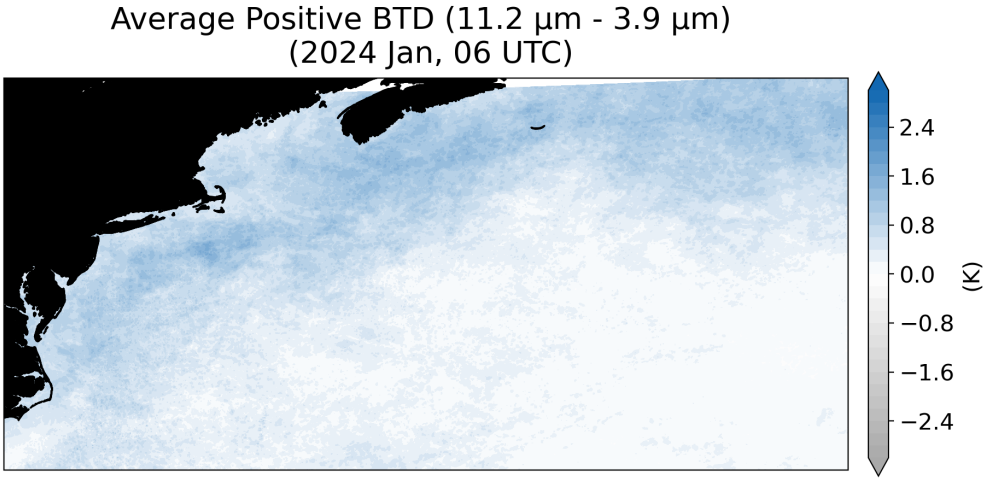

(b) Winter

Figure 3.14: (a) Average positive IR BTD in the Gulf Stream region during July 2024. Note how the positive measurements are weighted toward the northern side of the Gulf Stream in the summer. This is likely because of the higher frequency of FLC events, which require both cold water and warm air masses. Also, the ubiquitous Georges Bank FLC signal is visible near Cape Cod. (b) Average positive IR BTD in the Gulf Stream region during January 2024. Low cloud signals are more likely to be accurately dispersed during the winter, when FLCs on the cold (northern) side of the Gulf Stream are less common.

These case studies suggest that the consistently cold SST region in the Gulf Stream only needs the advection of a warm, moist air mass for the production of positive IR BTD and associated FLC signals. It has been shown anecdotally in Figure 3.11 that warmer southerly winds generate more visible eddy features in the IR BTD than colder northerly winds. And in the case of a known warm and moist air mass arriving over the cold part of the current, the positive signals in the IR BTD strongly increased. In Figure 3.13, it is shown how the positive signal extent matched the underlying cold SST, making it likely that many of these are FLCs.

Another region of strong SST gradient is along the warm Kuroshio current, where it meets the cold Oyashio current. This region has been previously identified as having FLCs (Gladkova et al., 2015). When warm, moist air is advected over, it is likely that the Kuroshio Current also displays visible eddies in the IR BTD.

It is worth noting that these synoptic scale and semi-persistent processes can lead to more widespread regions of potential FLCs compared to the localized and ephemeral nature of processes like Georges Bank and Oaxaca region. Thus, there are some parts of the world that may be predisposed to more robust biases in FLCs. Since these FLCs are often inherited into the SST masking algorithms, it is likely that some regional cold SSTs in warmer areas are being repetitively filtered out of the SST climatology, due to the supposed coverage of nighttime clouds. This overstatement of cloudiness on FLC-prone regions will likely cause a local warm biases in the SST climatology. This warm bias could cause downstream errors in fields like fishery management (regions of cold upwelling are often productive fisheries), climate model initialization (models need as accurate a current SST state as possible), or ocean dynamics (SST determines the density of the water).

In these case studies (Georges Bank, Oaxaca, and Gulf Stream), we have discussed three physical sources of warm and moist air over cold sea surfaces: 1) cold water upwelling due to underwater banks, 2) wind-driven cold water upwelling, and 3) currents creating strong SST gradients. In each of these scenarios, an SST cold pool is created near to warmer waters, where it is possible that warm moist air associated with the predominantly warmer regional maritime air mass will pass over the localized cold pool, setting up the right conditions for positive IR BTD signals.

With that said, there are other physical scenarios known to cause false cloud signals, such as river outflows pouring cold water into a warmer environment. For example, the Mississippi delta is specifically known to cause false cloud signals (Miller et al., 2022). Rapid radiative cooling is another potential cause, and has been shown to cause false clouds over the Great Lakes. Some coastal zones, such as the California coast, experience coastal upwelling with similar results. Combined with the new case studies of this research, we begin to realize the likelihood of other regions holding potential for similar effects, and yet additional disparate physical mechanisms that conspire to result in the right conditions for them to occur.

These regional and anecdotal cases do little to help determine the physical and temporal extent of events worldwide. Global knowledge of FLCs has implications not only to local and episodic effects but potentially to climatological impacts. In attempt to capture the patterns of FLCs on a larger scale and begin to form a mechanism for addressing these global-scale climatology questions, we developed the novel IR BTD simulation, developed and demonstrated in the next chapter of this thesis.

Chapter 4

FLC Simulations

In the previous chapter, we outlined the physical basis for FLC events and examined various case studies where they observed in nature. To anticipate future FLC events and assess their preferred zones of occurrence, we turn to simulations based on coupling the temperature and moisture profile of a numerical weather prediction (NWP) model to the governing radiative transfer equations for nighttime scenes in the shortwave IR and longwave IR bands that comprise the IR BTD. Using the radiative transfer methods outlined in Chapter 2.6, we created a model-driven simulation of FLC events.

Our simulations are dependent only on the water vapor and temperature profiles in the atmosphere that are resolved by the NWP model (GFS model in this study), coupled with ancillary information about the SST derived from composite satellite data. Therefore, these simulations will show the FLC signals only when the model itself resolves a moist inversion present above cool SST anomalies. An important implication here is that any low cloud present in the NWP model are not represented by this radiative simulation. Any positive IR BTD shown in the simulation corresponds to locations where water vapor may cause an overstatement of low cloud coverage. It does not mean that there are no low clouds in the region, only that the test is likely to see low clouds whether or not they exist in the model or in nature.

4.1 Simulation of IR BTD Imagery

The simulation of the IR BTD was built from GFS data (Chapter 2.3), NOAA Optimum Interpolation SST data (Section 2.4), and HITRAN molecular absorption data (Chapter 2.5). The simulation code is available at github.com/jesseturner/hitran_api/blob/main/FLCI.ipynb.

To conduct the radiative transfer simulations, we utilize water vapor extinction values derived from the HITRAN dataset, and apply these values to the water vapor mass density values from the GFS model to determine the total optical depth and thus the transmittance value from each level

to the top of the atmosphere. The change in transmittance with height represents the weighting function in Equation (2.13), and provides an indication of what levels of the atmosphere a given infrared measurement is sensitive to, under the assumption of a conservatively scattering media (i.e., Schwarzschild's Equation).

To convert the hyperspectral HITRAN data to a usable dataset for narrowband ABI simulations, the data were organized into a water vapor extinction coefficient look-up table. For each 0.001 wavenumber in the desired spectral range (determined from the ABI shortwave and longwave IR bands, respectively), the absorption coefficient was calculated under the assumption of Lorentz broadening (i.e., pressure and temperature dependencies are accounted for in the calculations). To get a result for each ABI band, the extinction values were averaged over the spectral band range (10.8 μm to 11.6 μm for ABI band 14 and 3.8 μm to 4.0 μm for ABI band 07), serving as a rudimentary sensor response function. A more detailed calculation based on weighting the spectra by the normalized spectral response function was not done here but is not expected to result in dramatically different results since neither of the ABI bands considered here reside near rapidly changing water vapor absorption features.

To apply the HITRAN-based water vapor extinction table to simulated radiances and brightness temperatures used for this study, GFS data were enlisted to generate a water vapor mass density profile for each location in a scene. Mass density (u, $\frac{\text{kg}}{\text{m}^2}$) is calculated between each pressure level using Equation (4.1), where r_g is the mixing ratio and p are the pressure levels, defined as follows:

$$u(p_1, p_2) = \frac{1}{g} \int_{p_1}^{p_2} r_g dp \tag{4.1}$$

In order to reconcile the units of the extinction table and mass density profiles, the absorption coefficient units of $\frac{\text{cm}^2}{\text{molec}}$ were converted to $\frac{\text{m}^2}{\text{kg}}$ using the mass of water. At this point, the extinction ($K(T, P)$) and mass density $u(T, P)$) were multiplied to result in a profile of optical thickness ($\tau(z)$). For each pressure level in the water vapor mass profile (21 vertical levels from the GFS model), the nearest temperature and pressure index was found from the extinction table (20 levels). The largest pressure difference between the two tables is 23 hPa, with most being much less.

The resulting optical thickness ($\tau(z)$) could then be used to calculate transmittance ($T_\lambda(z, \text{TOA})$) through the atmosphere (per Equation (4.2)). The change in transmittance over the change in height was used to calculate the weighting function.

$$T_\lambda(z, \text{TOA}) = \exp\left(-\sum_{z}^{\text{TOA}} \tau(z)\right) \tag{4.2}$$

Recalling Equations (2.11)-(2.13) expected at-satellite radiance ($I_\lambda^\uparrow$) includes both a surface term and the atmospheric term. The atmospheric term was calculated using the HITRAN and GFS data as described above. For the surface term we use the OISST data as the temperature and the total optical thickness (τ_λ^*) through the atmosphere (also determined from the HITRAN and GFS data).

Because of the nadir assumption made in Section 2.6, the viewing angle (μ) was set to unity, as if the satellite were directly over the location. Although a latitude-dependent calculation of viewing angle would be necessary for a head-to-head comparison with satellite observations, this simple nadir-assumption construct allows our simulation to be compared to various locations worldwide in a sensor-agnostic way. It should be noted, however, that off-nadir viewing geometries will result in a stronger contribution from the atmospheric term of Equations (2.11)-(2.13) in spectral bands where the atmospheric absorption is non-zero (in particular for the 11.2 μm band of ABI).

Thus, depending on the structure of the temperature and moisture profile, the IR BTD of off-nadir viewing will differ from a nadir result; given the peak of the 11.2 μm weighting function being in the boundary layer and at the surface, we would anticipate that for cases of FLC (warm and moist air over cool SST) the IR BTD may be slightly larger for the off-nadir viewing geometry compared to at nadir, since the atmospheric path through the lower atmosphere is geometrically longer (accentuating the lower atmospheric emission contribution). We will keep these caveats in mind when comparing simulated IR BTD to actual observations of such from GOES-16 ABI.

4.2 Evaluation of performance

Figure 4.1 shows a comparison between a measured (radiosonde) atmospheric profile and model (GFS) atmospheric profile for a region that was experiencing a positive IR BTD. An atmospheric sounding from Yarmouth Airport (YQI) in Nova Scotia, Canada was compared to the GFS model point at the same location (43.8° N, -66.1° W) and time (00:00 UTC). Figure 4.1a shows the radiosonde measured a warm and moist air mass over the region, at about 970 hPa. Figure 4.1b shows the GFS also captures a warm and moist air mass near 1000 hPa, although the magnitudes and structures differ. Both observation and GFS model identified the low-level air mass, but the GFS shows the inversion only very close to the surface, where the sounding shows this inversion to extend to higher altitudes in the lower atmosphere.

The current GFS model is known to have difficulty representing low level inversions (Sun et al., 2010). This causes, among other issues, the understatement of the stratocumulus layer, particularly over the subtropical Pacific Ocean. The bias is most prevalent at the very low altitudes (including the 2-m reporting level), and during the winter the model is shown to have a low-level warm bias at night (Patel et al., 2021). This issue with GFS planetary boundary layer parameterization schemes also tends to bias toward weaker hurricane formation (Zhang et al., 2020).

Since the warm and moist layer creates the FLC signals (Miller et al., 2022), this disagreement will directly affect the accuracy of the FLC simulations, which use the GFS data as input for the atmospheric temperature and moisture profile. In particular, the model's lower altitude placement of the warm moist layer will reduce the optical path of the emissive layer in the longwave IR simulations, resulting in the FLC simulation giving weaker BTD results than reality. The effect is further compounded by the nadir viewing assumption of the simulation compared to the actual GOES ABI viewing geometry, where the latter will traverse a longer optical path of warm and moist air. Due to these issues, the simulation likely generates a more conservative (less prominent) FLC field. Despite these issues, our radiative transfer equations on top of the current GFS model do well enough to produce a positive IR BTD in the same regions as the observed FLC events. Most

of the FLC cases also occur during the summer (discussed in Section 4.3, so the winter temperature bias is largely avoided.

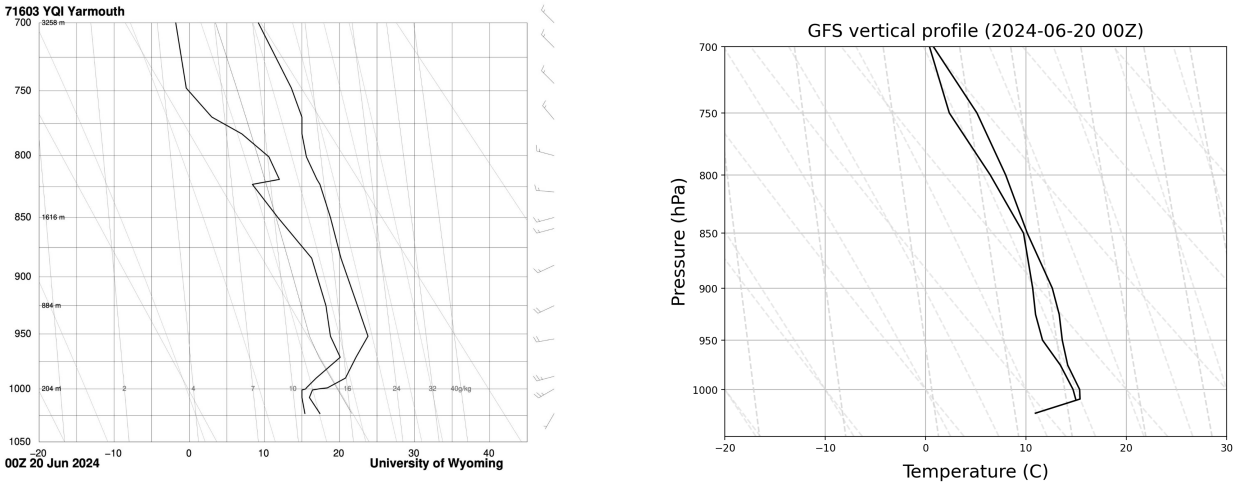

(a) **(b)**

Figure 4.1: (a) Atmospheric profile from the radiosonde launched from Yarmouth Airport in Nova Scotia. (b) Atmospheric profile of temperature and moisture from the GFS model. The GFS model uses pressure levels with 25 hPa or 50 hPa steps, the bottom level at 1010 hPa is GFS 2-m. The surface temperature at 1025 hPa is collected from the OISST. Notice that, where the radiosonde observations show a moist inversion, the GFS data shows a similar moist inversion closer to the surface.

Despite the caveats raised between the comparisons of simulated and observed IR BTD, Figure 4.2 shows the FLC simulated IR BTD capturing a similar spatial pattern to the GOES-measured IR BTD for a FLC event. Figure 4.2a shows the satellite imagery for the 11.2 μm - 3.9 μm BTD, which includes the water vapor-based FLC signals, but also includes actual low cloud signals (which produce a positive IR BTD owing to microphysical properties in the water droplets (Ellrod, 1995)). FLC can be differentiated from true low clouds in the ABI observations via animated imagery, possible from the geostationary platform, which reveals the FLC as stationary features tied to the mixing zones. The differentiation is difficult in static images, but using prior knowledge from Chapter 3.1 and Figure 3.7, it is not surprising to see the Georges Bank and Nantucket Shoals region highlighted as positive BTD in Figure 4.2a. The FLC simulation for the same time (Figure 4.2b) confirms the presence of the physical variables that FLCs. These images are also from

June, which is known to be one of the summer months most likely to show positive BTD over the banks. This all lends evidence that these signals are likely due to water vapor effects (FLCs).

We have also discussed the Gulf Stream as being susceptible to FLC events in Chapter 3.3, and it can be guessed that the swath of positive BTD (blue) from Cape Cod across Nova Scotia might be FLC, given the confirmation of water vapor effects from Figure 4.2b. The more distinct scattered shapes of positive BTD on the eastern and southern sides of Figure 4.2a are likely true low cloud. Recall that our simulations in Figure 4.2b contain only has the water vapor effects and do not include information about clouds, low nor high. The FLC simulation highlights the coastal swath from Cape Cod across Nova Scotia as positive BTD, providing further evidence that these features are indeed FLC signals produced by the warm and moist air over cool SST set-up.

Negative BTD values in the IR BTD (Figure 4.2a) can be caused by either overriding higher clouds or clear-sky regions of no-inversion. The region of strongly negative BTD (gray) along Maine seen in GOES ABI imagery is likely overriding higher clouds, identifiable by the distinct shape of the cloud edges. The weakly negative BTD region in the center of the image is likely a non-inversion, where the SST is simply warmer than the maritime air above it and causing a slightly depressed brightness temperature at 11.2 μm vs. 3.9 μm. This can be identified by the SST eddies noted in that region. As expected, the FLC simulation (Figure 4.2b) is able to see the negative BTD in the center of the image, but not the negative BTD from overriding high clouds (since clouds are not included in the simulations).

Figure 4.3a shows the IR BTD for the full scan of the GOES-E ABI. Large regions of known MBL cloud are highlighted as positive BTD, such as the western coasts of North and South America. These are likely true low cloud. Furthermore, these cloud features were observed to drift with the wind field at the levels of these clouds. There is an "edge" along the northeast corner of the image where there ceases to be any positive BTD anywhere in the scene. This is likely where the sun has risen and the reflective solar component is included in the 3.9 μm band. This has the effect of making the 11.2 μm - 3.9 μm BTD negative for all pixels, cloud and clear sky alike.

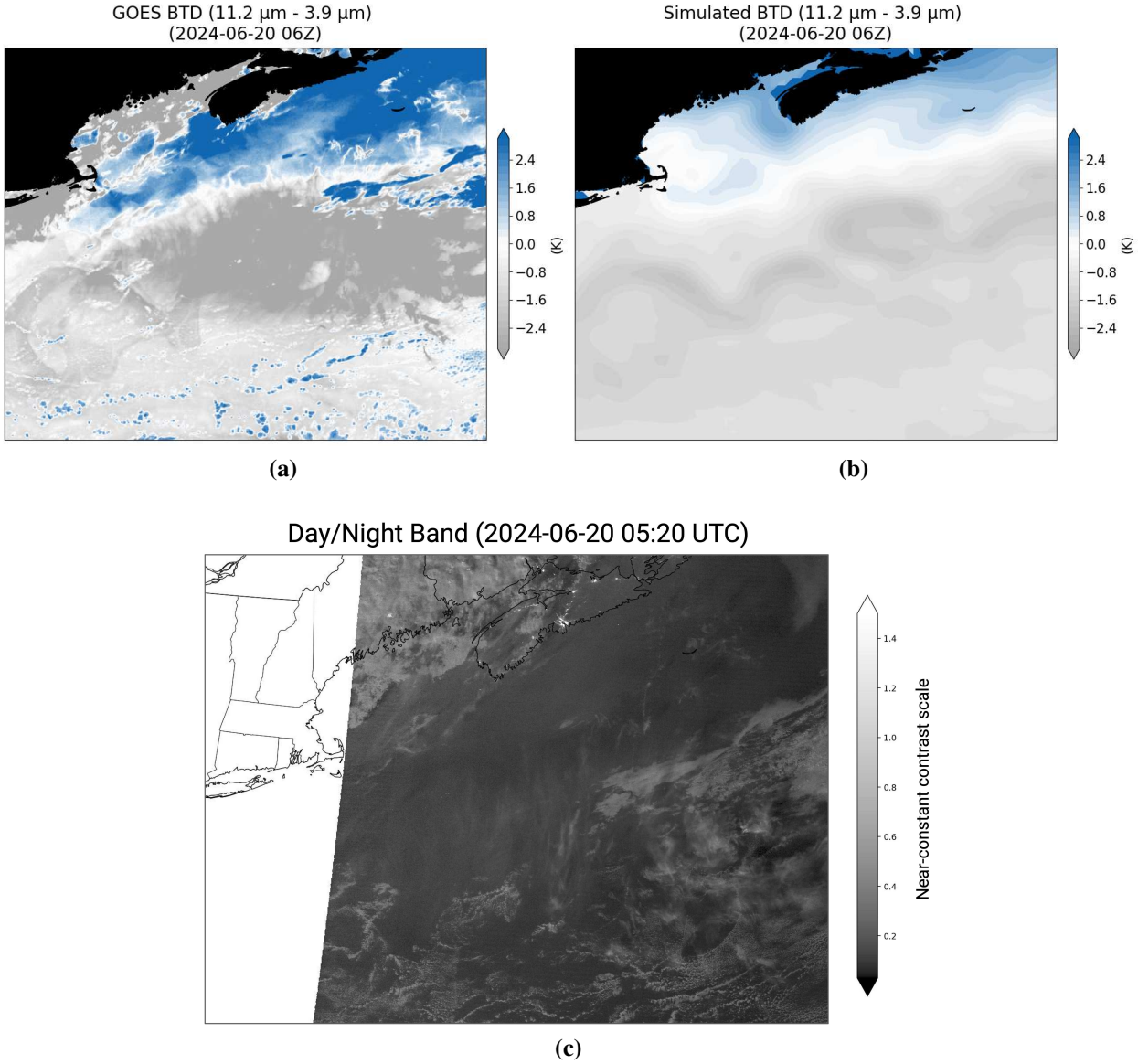

Figure 4.2: (a) The IR BTD as viewed by the GOES ABI, highlighting potential low clouds in blue. (b) The FLC simulation of the BTD, highlighting potential false low cloud signals in blue. The FLC simulation shows that the physical characteristics are in place for much of the low cloud extent to be largely FLC. (c) The Day/Night Band (with 98% moon illumination) shows some higher clouds near the coast, and some scattered low clouds near the south and east sides of the image, but no clouds along the main swath of positive IR BTD.

Figure 4.3b shows the FLC simulation for the full field of regard for GOES-16 ABI. The simulation agrees that most of the low clouds shown in Figure 4.3a are in fact true features, except for the region around the Northeast US and Atlantic Canada where the strong potential for FLC exists. Since we have previous evidence for FLC events occurring in the region for this case, these findings are encouraging in terms of the veracity of the FLC simulations.

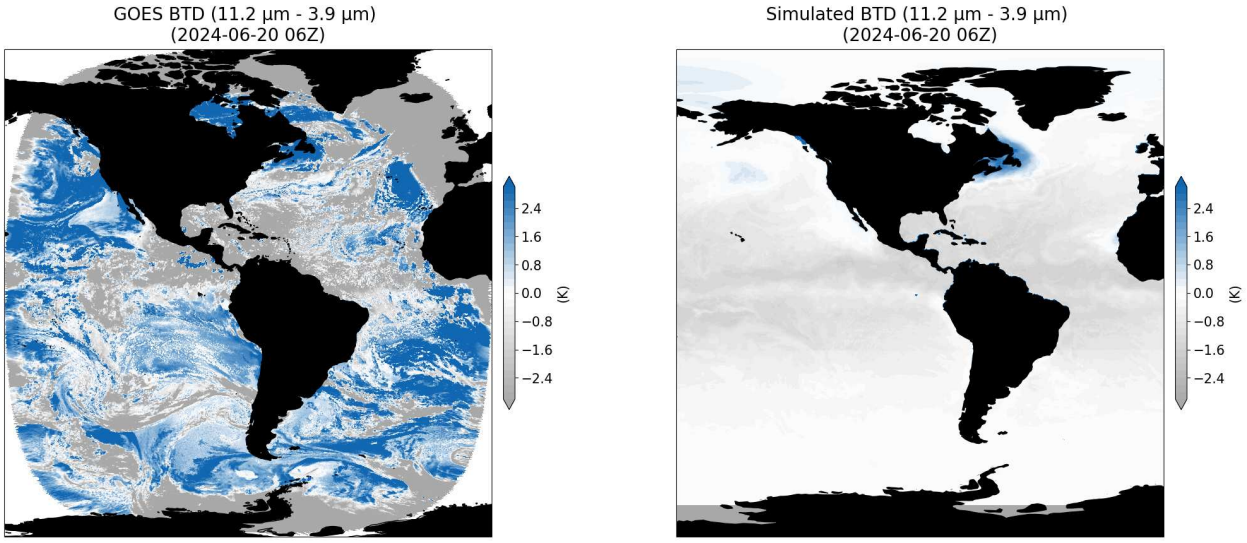

(a) **(b)**

Figure 4.3: (a) Full scan of GOES-E ABI nighttime low cloud field. (b) FLC simulation showing that only northeast North America exhibits the potential for FLC. Over-land pixels are not evaluated here, and are blacked-out in the imagery. The FLC simulation shows that the region near the Maine and Nova Scotia coast has the potential to be overstating the low cloud field.

4.3 Global patterns of simulated IR BTDs

By running the FLC simulation on the global scale, we can extend our analysis and attempt to identify regions that experience the meteorological conditions necessary to create false clouds. These conditions relate to both the atmospheric and surface conditions, per the radiative transfer derivations of Chapter 2.6. Limiting highlighting of the simulated imagery to positive IR BTD removes distraction of those regions experiencing normal cool and dry air over warmer surfaces, and helps to pinpoint regions of interest for FLC as well as locations where warm and moist

inversions may exist across the world's ocean. The latter may be useful for fog formation potential, radar ducting, and other possible applications.

Figure 4.4 shows the positive BTD from the FLC simulation for 12 July 2024 at 06:00 UTC. Although the BTD reached values of nearly $\sim$1 K, the range was limited for the ease of viewing the weaker potential FLC regions. We note that the only regions currently experiencing FLC signals in Figure 4.4 are in the upper latitudes of the Northern Hemisphere. This bias of signal toward the northern mid-latitudes for this case may be due to it being the boreal summer, when there are more warm air masses in the Northern Hemisphere. The lack of FLC signals in the lower latitudes is expected, due to the relative lack of cold SSTs. Without the cold surface (lower boundary), the conditions for the FLC signal are not present. From this discussion, we might infer that any possible SST climatological biases arising from FLC effects would be most prominent in the mid- to upper-latitudes of the boreal spring and summer hemisphere, with smaller, more ephemeral and seasonally agnostic signals at lower latitudes of both hemispheres associated with local upwelling events (e.g., Oaxaca example of Chapter 3.2).

The global-scale currents are frequently regions with sharp temperature gradients. The FLC simulation in Figure 4.4 highlights the northeast side of the Kuroshio Current. The Gulf Stream is not very distinct in this simulation run on 12 July 2024, but there are some of the ubiquitous FLC features near Georges Bank and Nova Scotia. That region could be highlighted due to the temperature gradient from the current, or the upwelling that occurs there, or both.

Figure 4.5 shows a composite of FLC simulations for the full month of July 2024. The image shows the average of the positive BTD taken at each day of the month at 06:00 UTC. Many of the regions of potential FLC signals are similar to Figure 4.4, with most signals occurring at the highest latitudes. This relates back to Figure 1.4, where Chirokova et al. (2023) notes the appearance of FLCs in the far-north regions of the ProxyVis product. Some transient features from the 12 Jul 2024 case have disappeared in the average, including the subtle FLCs east of New Zealand. The extent of the Kuroshio Current FLC has retreated back to the steepest temperature gradient in the average. Many of the previously known regions of FLC (California coast, Georges Bank, the

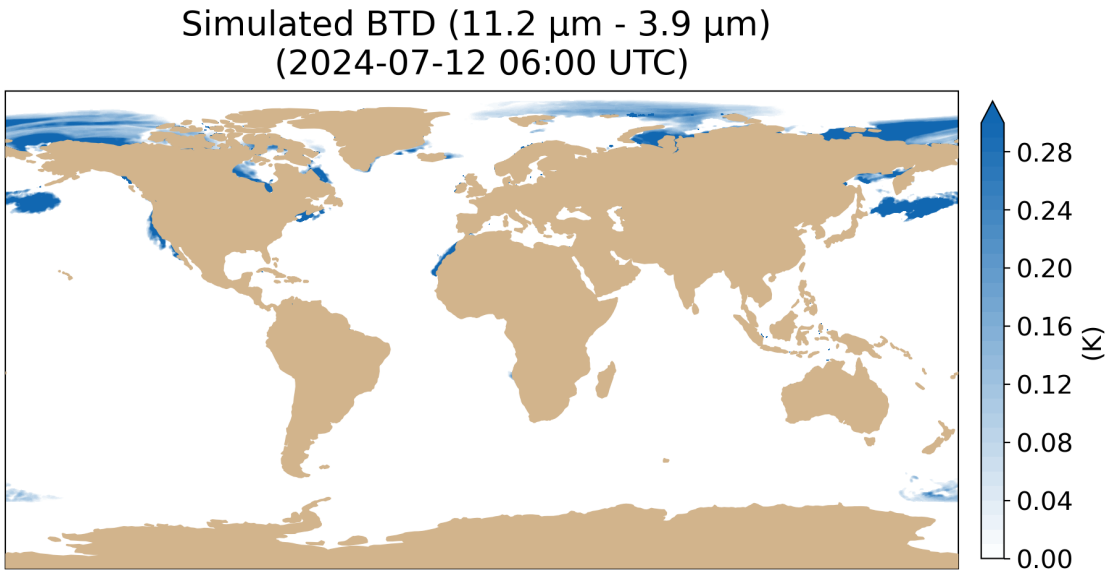

Figure 4.4: The false low cloud simulation ran on a global scale for 12 July 2024 06:00 UTC. The regions highlighted are experiencing a strong low-level moist inversion that will cause a positive signal in the infrared difference observations. Standard low cloud tests and associated cloud masks will likely show false positives in these regions, overestimating cloud coverage.

Kuroshio Current) appear in the average simulation for July 2024. The western coast of Northern Africa, the coast of Newfoundland, Hudson Bay, and the Arctic Ocean are all regions that would likely benefit from FLC investigation in the future.

It is worth noting that the false positives in the IR difference will have greater impact on the half of the Earth experiencing nighttime. Some operational uses of the IR BTD switch to visible spectrum imagery during the day, nullifying the FLC issue. This is the case for the ACSPO clear-sky mask (Petrenko et al., 2009), which uses both reflectance and thermal tests. However, if a cloud mask model were to be trained on IR BTD data, with the attempt to be agnostic to daytime and nighttime, it would be likely to inherit FLC errors into the daytime.

In Figure 4.4 and Figure 4.5, the FLC simulations were run for 06:00 UTC, which is nighttime for most of the Western Hemisphere. Although the true IR BTD does not apply to the daytime, due to the reflective sunlight component in the 3.9 µm band, the FLC simulation is able to show both day and night (since the solar term is not included in the radiative transfer equation). Although the FLC simulation can be run on regions in the daytime, the differing radiative scenario may change

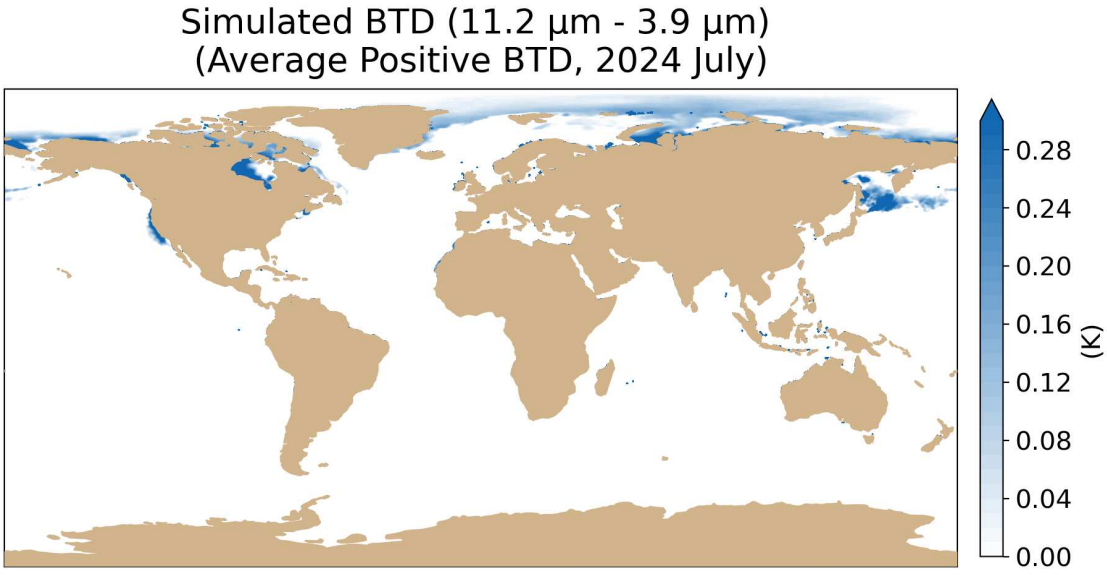

Figure 4.5: The global false low cloud simulation average positive values for the month of July 2024. Each day in the month was run for 06:00 UTC. Note that the FLC regions congregate in the Northern Hemisphere due to the summer season. The California coast, Georges Bank, and Kuroshio current have all been previously noted as potential FLC areas in this research. These regions of repetitive FLC potentially lead to SST warm biases by filtering-away valid cold SST retrievals in these regions.

the rate of potential FLC signals. Since the atmosphere is largely transparent to sunlight, and the ocean surface has a low albedo and is absorbent to sunlight, daytime is likely to warm the SSTs faster more than the air masses above. This temperature change from night to day in the SST and atmospheric profile would lead to the FLC simulation underestimating FLCs for the daytime part of the world. On the other hand, the cold pools present during the day are generally present at night, so any regions highlighted for FLCs during the day will likely show those signals even stronger at night.

Although infrequently done due to the availability of visible spectrum imagery, one could plausibly use the IR BTD to look for maritime cloud extent during the day. The daytime IR BTD experiences extreme negative BTDs from clouds (instead of positive for low clouds at night), due to the shortwave IR being sensitive to solar reflectance. However, the clouds are often distinct from the ocean, which is low albedo and usually shows up closer to zero on the IR BTD. Exceptions exist for ocean sunglint and wavy regions, which show a strong negative IR BTD similar to clouds. Atmospheric reflection off of aerosol would also add to the solar component in the shortwave IR.

Another disadvantage of using a daytime IR BTD is the lack of differentiation between high and low clouds, which both show up in the negative. Due to the impracticality and completely different mechanics of a daytime IR BTD, we do not compare any daytime measurements to the daytime FLC simulations.

Although not limited by daytime vs. nighttime, the FLC simulation is limited by the 1/4° ($\sim$28 km at the equator) horizontal resolution shared by the GFS model and the OISST data. GOES ABI imagery has a higher spatial resolution of 2 km for the infrared bands (GOES-R; https://www.goes-r.gov/spacesegment/abi.html). The VIIRS imagery also has a higher resolution of 0.75 km (VIIRS, NASA; https://ladsweb.modaps.eosdis.nasa.gov/missions-and-measurements/viirs/). It is very possible that there are false cloud events appearing on satellite imagery that are too small to be visualized with the FLC simulation. This is especially likely for regions of very localized cold pools of SST, like small river outflows.

As shown in Figure 4.1, the FLC simulation captures the inversion closer to the surface than the measured sounding data. This is partially due to the aforementioned issues with the GFS struggling to resolve low-level inversions, but also due to the limited vertical resolution of the model. From 1000 hPa to 900 hPa, the model uses a 25 hPa resolution, which becomes coarser in the higher atmosphere. The GFS model also provides a 2-m reporting level. With the addition of the SST, there are only six layers of resolution in the lower atmosphere that are available to capture moist inversions. This resolution may be sufficient for strong inversion cases that span multiple layers, but the FLC simulation may miss thin warm and moist air masses that could have influenced the radiative transfer simulations if they were accounted for.

On the global scale, the FLC simulation highlights geophysical patterns, such as large currents and regions of extensive deep-water upwelling. On small regions, the FLC simulation tends to outline more specific features in the SST, like bank edges and eddies. Used on short time scales, the FLC simulation highlights a snapshot of the current environmental state, which is useful for anticipating transient false low clouds. Running the simulation on longer time scales, and aggregating data statistically, is better for capturing persistent regions of FLC that may introduce biases

to downstream products (cloud masks, and other products reliant on the cloud masks) which depend on the IR BTD. The FLC simulation was developed in order to understand and fix errors in the IR BTD, but next we will discuss how the simulation has potential to be used in a predictive fashion.

Chapter 5

Discussion

5.1 Alternative methods of removing FLCs

An important caveat to interpreting FLC patterns is that not all longwave and shortwave IR channels are centered on the same wavelengths. The ABI instrument has 3.9 μm in the SWIR and both 11.2 μm and 10.3 μm available in the LWIR. In contrast, the AVHRR/3 instrument uses 3.7 μm for shortwave IR 12 μm for longwave IR. The VIIRS instrument has three shortwave IR bands and three longwave IR bands, with users tending to employ the bands centered at 11.45 μm and 3.74 μm for the nighttime low cloud test. Although ostensibly similar, these slightly different bands do not behave exactly the same in the radiative transfer, owing to subtle variations in the water vapor absorption spectrum. For example, the 10.3 μm band tends to be the "cleanest window" to water vapor (i.e., weakest water vapor absorption, so, seeing mostly the surface emission), with the least absorption compared to the "dirtier windows" of 11.2 μm, 11.45 μm, and 12 μm. Since these dirtier longwave IR windows experience more water vapor absorption effects and, by Kirchhoff's Law, also emit more compared to the cleaner shortwave IR, IR BTD products based on 11.2 μm, 11.45 μm, and 12 μm may exhibit stronger FLC compared to products derived from 10.3 μm, for cases when the FLC-conducive environmental conditions are in place.

In Gladkova et al. (2015), a SST pattern test is applied to the ACSPO clear sky mask (ACSM) to identify FLC features in the algorithm. Acknowledging that human users tend to be able to identify FLCs, this study uses the processes of the human eye by focusing on the local contrasts, ratios, and gradients in an image. This is achieved with a SST pattern test, which identifies supposedly cloudy regions with SST gradient ridges (similar to thermal fronts) and a retrieved SST colder than the reference SST, then applies a series of shape-based tests to determine if it is likely to be false low cloud. Results from the test increased the global clear-sky field by 0.2 - 0.3%. In dynamic ocean areas and coastal zones, the SST pattern test decreased false low clouds in the ACSM by as

much as 15%. The study of Gladkova et al. (2015) is different from our approach in that it only uses the SST data ingested into the ACSM, and removes FLC signals without need for data on the atmospheric state. Our approach in this study uses SST data with surface observations and GFS data to simulate the atmospheric thermal emission and identify regions of FLC risk. Despite this, both approaches show localized regions of repeated FLC events and agree on various locations, including the Gulf Stream and the Kuroshio Current. A useful direction of future research would be to examine the commonalities between the SST pattern test, our simulated FLC data, and FLC observations.

Gladkova et al. (2015) agrees that FLCs tend to occur near strong SST gradients. However, due to the focus away from the atmospheric composition, Gladkova et al. (2015) suggests an alternative explanation for the FLC features in the cloud mask. The ACSM uses dual SST fields: a reference daily SST field and an instantaneous retrieved SST field. The first is used to generate cloudy and clear clusters by detecting unrealistically cold SSTs, the second for refining their boundaries by analyzing statistics of clear and cloudy pixels within the neighborhood of the tested pixel (Petrenko et al., 2010). The differences between the reference SST field and retrieved SST field at strong gradients is cited as the cause for FLCs near strong currents, cold upwellings and eddies (Gladkova et al., 2015). It is likely that this explanation encompasses the physical description given in this research, by way of the atmospheric dynamics being incorporated into the differences between the SST fields.

5.2 Determining fog potential from FLCs

Whereas the emphasis of this research has been on the possibility of positive IR BTDs corresponding to clear sky moist inversions atop cool SSTs, it is important to note that advection fog can form in the same warm-moist air over cold sea surface environments that cause the FLC signals, due to cloud-top radiometric differences between the shortwave IR and longwave IR bands. Fog in the US west coast has long been observed as the saturation of warm air when advected over a colder sea surface (Koračin and Dorman, 2017). As shown in Figure 4.4, the US west coast is also

a region that frequently experiences water vapor-based positive IR difference signals, for the same reason. Thus, having an independent measurement of the scene, such as moonlight reflectance from the DNB, or a lidar based measurement, is an important element to real-time analyses of these regions. As noted, some aspects of the geostationary observing platform can also be leveraged to help disentangle false and true low cloud features via feature consistency considerations.

In particular, Georges Bank, fog has been observed forming over the region known for FLC cases. During the summer, Georges Bank and Nantucket Shoals consistently show a distinctive positive IR BTD, but on 28 July 2020, this structure was blurred by a true low cloud signal. Figure 5.1 (Line, 2020) shows the region developing advection fog during the day, then showing both the FLC and true low cloud signals co-occurring in the IR BTD after sundown. The result at night is a version of the usual Georges Bank FLC pattern that has been blurred by the addition of true low cloud created in the region. The blurring is due to the motion of the fog over the course of the evening, since it does not dissipate immediately upon drifting away from its formation location.

Thus, the existence of a weakly positive IR BTD signal does not necessarily mean there is no true low cloud in the region. Since advection fog often forms in false low cloud conditions, theoretically the FLC simulation can also be considered as a "fog potential" product. Regions with simulated positive IR BTD are indicative of warm moisture over a relatively cooler sea surface, and that moisture can condense into cloud if the conditions are favorable.

A similar effect can happen in the converse, where cold air blowing over warm surface causes boundary layer deepening and incipient convection via instability (Klein and Hartmann, 1993). This process occurs over warm currents, such as the Gulf Stream and The Kuroshio current (Gladkova et al., 2015). Clouds generated by this method are likely to be adjacent to areas of interest to our research, instead of directly over the false low cloud signal, since the atmosphere and surface attributes are "flipped" compared to the ideal FLC conditions.

An advantage of the FLC simulation is that it is not hampered by overriding cirrus. In the nighttime low cloud test, ice clouds above either true or false low clouds will obscure the positive BTD signal and impart a strong negative BTD. This effect is due to the dramatically higher absorption of

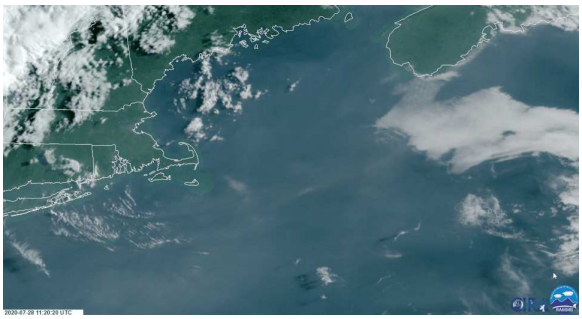

(a) GeoColor (28 July 2020 11:20 UTC)

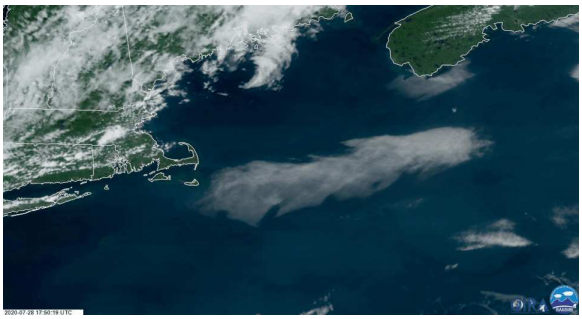

(b) GeoColor (28 July 2020 17:50 UTC)

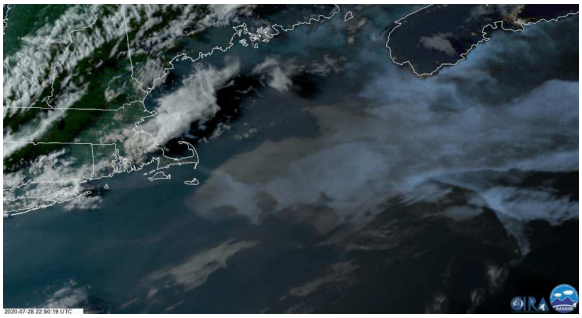

(c) GeoColor (28 July 2020 22:50 UTC)

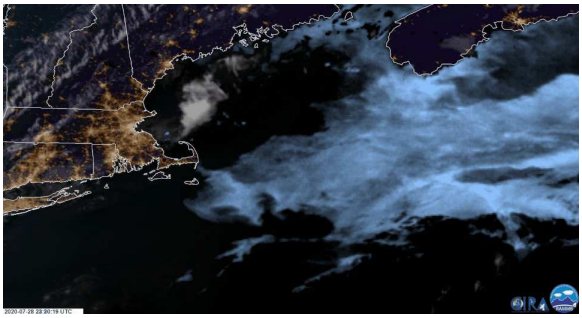

(d) GeoColor (28 July 2020 23:20 UTC)

Figure 5.1: (a) Daytime GeoColor imagery of Georges Bank prior to the formation of advection fog. (b) Advection fog forming over the relatively cold waters of the Georges Bank region. (c) GeoColor daytime and nighttime imagery as the terminator crosses, showing the extent of the true advection fog overlapping the distinctive shape of the more expansive FLC signal across the region. (d) Nighttime GeoColor (blue, with intensity indexed to the magnitude of the IR BTD) showing both true and false low cloud signals. Case adapted from Line (2020), images from CIRA-SLIDER (https://rammb-slider.cira.colostate.edu)

ice crystals at 11.2 μm compared to 3.9 μm, leading to very cold 11.2 μm brightness temperatures from the high altitude (cold) cirrus due to their absorption and re-emission of upwelling radiation from the lower atmosphere and surface. Since the FLC simulation does not include clouds, only moisture and temperature, the patterns shown in the simulated FLC signals are not confused by patterns of overriding cirrus that are often present in actual observations of the IR BTD. When comparing the FLC simulation to observed products using the IR BTD, the simulation will show water vapor effects that may currently be covered by higher clouds. In a hypothetical "fog potential" application, this information could be a useful way of anticipating fog-forming regions that are currently out-of-sight due to cloud coverage. However, one must always remember that the simulated data are only as accurate as the model supplying the atmospheric temperature and moisture profile information.

5.3 Future research directions

In order to actualize a "fog potential" product based on the radiative transfer methods used to generate the FLC simulation, the relationship between FLC environment conditions and fog generation must be solidified. There is some evidence that moist low-level inversions are associated with sea fog (Yun and Ha, 2022), but it is unknown how a retrieval could be made to convert the simulated brightness temperatures to a quantity of expected fog. Complications arise due to the single variable of BTD relating to the many variables of fog, including vertical and horizontal extent, density, and time of formation and dissipation. That said, there is potential to develop a product for short-term forecasts of low-visibility regions over the ocean, incorporating FLC knowledge into the data framework. This theoretical product would have military and maritime transportation applications.

Another next step for this research is building of a climatology of global FLC regions. Low cloud climatologies from satellite are important due to the scarcity of ocean-based cloud measurements, which tend to congregate around major shipping lanes. Understanding the horizontal extent of these low cloud regions is also used for determining the time it will take to dissipate after

sunrise. These low cloud climatologies are currently hindered by FLCs, and the FLC simulation could be leveraged to determine the full extent of FLC events on a global scale (temporally and spatially). This would help determine the regions that are most vulnerable to overstating the low cloud extent, and if there is a seasonality to their FLC coverage. As discussed in Chapter 1, SST masking products are likely introducing a bias to the SST record due to repetitive errors in the IR BTD. A FLC climatology could be used to help determine the extent of these errors and estimate the local and global impacts on the SST record.

A more direct move toward application could be applying this simulation method to improve products dependent on the IR BTD. These products are used for notifying aviation and maritime operations of low-visibility regions, and any improvements will have direct positive impact on these users. Ingesting OISST and GFS model data into a cloud product and applying the radiative transfer methods from Chapter 2.6 would allow a product to know internally where the water vapor, SST, and temperature are primed to create a positive low cloud signal. A cloud product would then flag any low cloud measurements in the region as "potential FLC".

Chapter 6

Conclusions

This research aimed to investigate the physical causes and patterns of false nighttime cloud signals in satellite observations, and present a method using numerical model data and radiative transfer simulations to estimate the effects of atmospheric and oceanic conditions that can potentially lead to false cloud signals in satellite data. These two focuses worked in tandem for the overall goal of improving our understanding of FLCs and supporting more accurate nighttime cloud detection.

6.1 Summary: FLC physical causes

This study has presented FLC cases as a way to provide deeper insight into the physical causes of FLC events, including those mentioned by Miller et al. (2022). Through the case studies gathered from Georges Bank, Oaxaca, and the more general Gulf Stream region, we have highlighted a variety of physical patterns which can cause false positives in the nighttime low cloud test. The Georges Bank and Nantucket Shoals region develops a cool SST anomaly compared to surrounding waters due to the undersea shelf mechanically mixing cold water upward during tidal changes. Since this region is surrounded by warmer unmixed waters, warm and moist air masses associated with the predominant warm waters may oftentimes drift over the cool SST anomaly region, setting up the base conditions for producing FLC signals (positive IR BTD).

In an entirely different process discovered by this research, the southern coast of Oaxaca produces a FLC signature. Our analysis showed that this region experiences strong northerly mountain-gap winds which transport the warm surface waters offshore. These waters are replaced by deep and cold upwelling water, creating a local cool SST anomaly surrounded by warmer and moist air masses, producing local conditions similar to those of Georges Bank.

The Gulf Stream has been identified in previous studies as a region where it is frequently difficult to separate clear ocean from cloud at night (e.g., Gladkova et al., 2015). Our own analysis

shows that there may be an association between the prevailing wind direction and the appearance of FLC signals there. Specifically, when the prevailing wind blows warm air from the south or southwest, FLC signals begin to appear over any cool SST features present across the region.

6.2 Summary: FLC simulation

In order to better understand the extent of FLCs on a global scale, FLC simulations were developed to recreate how a nadir-viewing satellite radiometer providing the IR BTD capability would measure the water vapor effects in the scene. This simulation ingested OISST, which uses satellite and surface-based (e.g., buoy) sources to create an interpolated cloud-free global SST dataset. The simulation utilizes GFS model data for its global atmospheric temperature and humidity profile information.

The HITRAN molecular absorption database was consulted to determine the magnitude of water vapor emission in the shortwave and longwave IR bands of interest. Details of these radiative behaviors are both temperature and (especially) pressure dependent. A version of Schwarzschild's Equation was derived to determine the expected radiance, given the wavelength, surface temperature, and the weighting function through the atmospheric column. Then the Planck Function was utilized to calculate brightness temperatures for the shortwave and longwave IR bands, and from these, the IR BTD.

The result of the above method is a novel global simulation tool, applicable to the extent of the GFS and OISST records. The simulation tool returns positive IR BTD measurements when the environment is capable of producing a FLC signal—i.e., in conditions of sufficient warm and moist air overriding a relatively cool ocean surface. It is worth noting that the limitations in the GFS model and OISST, discussed in Chapter 4, are inherited into the FLC simulation, so uncertainties in these fields are inherited by the tool. This limitation is particularly relevant to the GFS data, since NWP models can struggle with boundary layer representation (discussed in Chapter 4.2)

Run globally, the FLC simulation highlights many of the known areas of FLCs (Georges Bank, California coast, Kuroshio Current) as well as revealing new areas of potentially overstated low

cloud coverage at night. Based on the results from a boreal summer run of the simulations, we have identified additional areas at risk of FLC errors: the western coast of Northern Africa, the Canadian coasts of Newfoundland and Hudson Bay, and the Arctic Ocean. The global use of the FLC simulation has also reinforced the assertion that FLC events tend to occur in the local summer, and at higher latitudes. This follows the logic outlined in our physical explanations, as this scenario provides the warm and moist air masses and strong SST gradients.

6.3 Summary: Impact and future work

In summary, and revisiting the fundamental science questions of this work, we have arrived at the following conclusions:

1. **What are the specific underpinning physical processes of these various phenomena?**

    - Through our deep-dive analysis of multiple case studies, we found that tidal mixing from underwater banks, mountain gap winds, and simple current transport can all generate localized regions of relatively cool SST (reduced by at least $\sim$5 K) compared to the surrounding SST field.
    - In particular, these processes each lead to producing the scenario of a cool lower boundary underlying a relatively warm and moist boundary layer air mass. When the sharp SST gradients (e.g., $\sim$0.1 K/km) generated by these mechanisms occur in temperate regions, the stage is set for positive IR BTD and more frequent occurrences of the FLC effect.

2. **Where, when, and how do these FLC processes occur in nature?**

    - Examining these case study regions in more detail, we found that many sharp SST gradients have clear seasonal dependencies. These temporal characteristics are unique to the area in question, and can lead to seasonally-dependent biases in cloud and cloud-dependent climatological parameters.

- For example, the Georges Bank region SST gradient is strongest in summer ($\sim$0.1 K/km), whereas the Oaxaca region is strongest in winter ($\sim$0.07 K/km). However, we have also found that the warm and moist air, an essential ingredient to FLC development, is often more prolific during the summer season.

3. **To what extent can we anticipate the development of these processes globally?**

   - A FLC simulation was developed to estimate FLC cases, based on the data from the GFS model and OISST observations applied to a radiative transfer model that takes into account the spectrally-dependent behavior of water vapor absorption (which gives rise to non-zero values of the IR BTD).
   - We found that, despite some issues with the GFS model's inherent ability to resolve the strength of low-level inversions, our simulations are able to successfully recreate the IR BTD based on water vapor effects well enough to identify areas of FLC interest.
   - Preliminary results (Figure 4.4 and Figure 4.5) show not only regions of known prolific FLC (e.g., the Georges Bank region and off the California coastal upwelling zone), but point to additional regions (e.g., northeast of Japan, coastal northwest Africa, parts of the Southern Ocean) where maritime low clouds may currently be overstated.
   - Examining these regions in detail, including their potential effects on the over-masking of valid SSTs, outlines a scope of future research that could hold regional implications to our present-day understanding of regional SST climatology.

The results from the case studies and global FLC simulations can help climatologists and forecasters determine the dependability of their tools for certain regions and times. The patterns and tools described in this work lend insights toward which physical regions are prone to false alarms and which regions are more reliable for cloud detection.

This research, and particularly leveraging of the FLC simulation tool, provides multiple new avenues for future research. It has been proposed that the filtering of FLCs in SST products likely causes a bias in the record. Investigating this issue could improve climate research that depends

on the accuracy of the SST record on regional to global scales as well as seasonal dependencies to these biases. To this end, another potential development is the creation of a global FLC climatology. This would allow forecasters and other users to know if their region of interest tends to experience FLCs at any point in the year.

More directly, the FLC simulation could be applied to existing satellite-derived products dependent on the IR BTD, making them more resilient against FLC errors. This research could also be extended to continental FLCs in the IR BTD. Although the mechanisms of FLC production are thought to be different, understanding these over-land FLC cases would greatly benefit the cloud coverage body of knowledge while improving near real-time imagery tools used by forecasters in time-critical operating environments.

Bibliography

J. W. Bergman and M. L. Salby. The role of cloud diurnal variations in the time-mean energy budget. *Journal of Climate*, page 1114–1124, 1997. doi: 10.1175/1520-0442(1997)010<1114:TROCDV>2.0.CO;2.

S. Bony and J.-L. Dufresne. Marine boundary layer clouds at the heart of tropical cloud feedback uncertainties in climate models. *Geophysical Research Letters*, 2005. doi: 10.1029/2005GL023851.

D. B. Chelton, M. H. Freilich, and S. K. Esbensen. Satellite observations of the wind jets off the pacific coast of central america. part i: Case studies and statistical characteristics. *Monthly Weather Review*, pages 1993–2018, 2000. doi: 10.1175/1520-0493(2000)128<1993:SOOTWJ>2.0.CO;2.

G. Chirokova, J. A. Knaff, M. J. Brennan, R. T. DeMaria, M. Bozeman, S. N. Stevenson, J. L. Beven, E. S. Blake, A. Brammer, J. W. Darlow, M. DeMaria, S. D. Miller, C. J. Slocum, D. Molenar, and D. W. Hillger. Proxyvis—a proxy for nighttime visible imagery applicable to geostationary satellite observations. *Weather and Forecasting*, 2023. doi: 10.1175/WAF-D-23-0038.1.

X. Dong, B. Xi, and P. Wu. Investigation of the diurnal variation of marine boundary layer cloud microphysical properties at the azores. *Journal of Climate*, page 8827–8835, 2014. doi: 10.1175/JCLI-D-14-00434.1.

D. I. Duncan, C. D. Kummerow, B. Dolan, and V. Petković. Towards variational retrieval of warm rain from passive microwave observations. *Atmospheric Measurement Techniques*, pages 4389–4411, 2018. doi: 10.5194/amt-11-4389-2018.

G. P. Ellrod. Advances in the detection and analysis of fog at night using goes multispectral infrared imagery. *Weather and Forecasting*, pages 606–619, 1995. doi: 10.1175/1520-0434(1995)010<0606:AITDAA>2.0.CO;2.

A. J. Fultz and W. S. Ashley. Fatal weather-related general aviation accidents in the united states. *Physical Geography*, pages 291–312, 2016. doi: 10.1080/02723646.2016.1211854.

I. Gladkova, Y. Kihai, A. Ignatov, F. Shahriar, and B. Petrenko. Sst pattern test in acspo clear-sky mask for viirs. *Remote Sensing of Environment*, pages 87–98, 2015. doi: 10.1016/j.rse.2015.01.003.

M. D. Goldberg, H. Kilcoyne, H. Cikanek, and A. Mehta. Joint polar satellite system: The united states next generation civilian polar-orbiting environmental satellite system. *Journal of Geophysical Research: Atmospheres*, page 13463–13475, 2013. doi: 10.1002/2013JD020389.

I. Gordon, L. Rothman, R. Hargreaves, R. Hashemi, and E. Karlovets. The hitran2020 molecular spectroscopic database. *Journal of Quantitative Spectroscopy and Radiative Transfer*, page 107949, 2022. doi: 10.1016/j.jqsrt.2021.107949.

J. E. Hansen and L. D. Travis. Light scattering in planetary atmospheres. *Space Science Reviews*, pages 527–610, 1974. doi: 10.1007/BF00168069.

D. L. Hartmann. *Radiative Effects of Clouds on Earth's Climate*. Academic Press, 1992.

D. L. Hartmann. *Global Physical Climatology: Second Edition*. Elsevier, 2016.

D. L. Hartmann, M. E. Ockert-Bell, and M. L. Michelsen. The effect of cloud type on earth's energy balance: Global analysis. *Journal of Climate*, page 1281–1304, 1992. doi: 10.1175/1520-0442(1992)005<1281:TEOCTO>2.0.CO;2.

A. K. Heidinger, A. T. Evan, M. J. Foster, and A. Walther. A naive bayesian cloud-detection scheme derived from calipso and applied within patmos-x. *Journal of Applied Meteorology and Climatology*, page 1129–1144, 2012. doi: 10.1175/JAMC-D-11-02.1.

J. Hrisko. Goes-r satellite latitude and longitude grid projection algorithm. https://makersportal.com/blog/2018/11/25/goes-r-satellite-latitude-and-longitude-grid-projection-algorithm, November 2018.

G. Hunt. Radiative properties of terrestrial clouds at visible and infra-red thermal window wavelengths. *Quarterly Journal of the Royal Meteorological Society*, pages 346–369, 1973. doi: 10.1002/qj.49709942013.

S. Kalluri, C. Alcala, J. Carr, P. Griffith, W. Lebair, and D. Lindsey. From photons to pixels: Processing data from the advanced baseline imager. *Remote Sensing*, pages 1–28, 2018. doi: 10.3390/rs10020177.

S. A. Klein and D. L. Hartmann. The seasonal cycle of low stratiform clouds. *Journal of Climate*, page 1587–1606, 1993. doi: 10.1175/1520-0442(1993)006<1587:TSCOLS>2.0.CO;2.

J. M. Klymak, S. E. Allen, and S. Waterman. Separation of an upwelling current bounding the juan de fuca eddy. *Journal of Geophysical Research: Oceans*, 2023. doi: 10.1029/2023JC019688.

R. Kochanov, I. Gordon, L. Rothman, P. Wcisło, C. Hill, and J. Wilzewski. Hitran application programming interface (hapi): A comprehensive approach to working with spectroscopic data. *Journal of Quantitative Spectroscopy and Radiative Transfer*, pages 15–30, 2016. doi: 10.1016/j.jqsrt.2016.03.005.

M. Konda, N. Imasato, K. Nishi, and T. Toda. Measurement of the sea surface emissivity. *Journal of Oceanography*, pages 17–30, 1994. doi: 10.1007/BF02233853.

N. Kopeika, A. Zilberman, and Y. Yitzhaky. Imaging through the atmosphere. *Reference Module in Earth Systems and Environmental Sciences*, pages 661–678, 2014. doi: 10.1016/B978-0-12-409548-9.09053-9.

D. Koračin and C. E. Dorman. *Marine Fog: Challenges and Advancements in Observations, Modeling, and Forecasting*. Springer, 2017.

K. Lau and H. Wu. Warm rain processes over tropical oceans and climate implications. *Geophysical Research Letters*, 2003. doi: 10.1016/j.rse.2004.06.004.

T. F. Lee, F. J. Turk, and K. Richardson. Stratus and fog products using goes-8–9 3.9-um data. *Weather and Forecasting*, pages 664–677, 1997. doi: 10.1175/1520-0434(1997)012<0664:SAFPUG>2.0.CO;2.

C. K. Liang, S. Mills, B. I. Hauss, and S. D. Miller. Improved viirs day/night band imagery with near-constant contrast. *IEEE Transactions on Geoscience and Remote Sensing*, pages 6964–6971, 2014. doi: 10.1109/TGRS.2014.2306132.

B. Line. Georges bank and low clouds. https://satelliteliaisonblog.com/2020/08/04/georges-bank-and-low-clouds/, 2020.

K. N. Liou. *An Introduction to Atmospheric Radiation: Second Edition*. Elsevier, 2002.

J. W. LODER and D. A. GREENBERG. Predicted positions of tidal fronts in the gulf of maine region. *Continental Shelf Research*, pages 397–414, 1986. doi: 10.1016/0278-4343(86)90080-4.

T. P. Mavor and J. J. Bisagni. Seasonal variability of sea-surface temperature fronts on georges bank. *Deep Sea Research Part II: Topical Studies in Oceanography*, pages 215–245, 2001. doi: 10.1016/S0967-0645(00)00120-X.

E. P. McClain, W. G. Pichel, and C. G. Walton. Comparitive performance of avhrr-based multichannel sea surface temperatures. *Journal of Geophysical Research*, pages 587–601, 1985. doi: 10.1029/JC090iC06p11587.

M. Messié and F. P. Chavez. Nutrient supply, surface currents, and plankton dynamics predict zooplankton hotspots in coastal upwelling systems. *Geophysical Research Letters*, 2017. doi: 10.1002/2017GL074322.

S. Miller and R. Turner. A dynamic lunar spectral irradiance data set for npoess/viirs day/night band nighttime environmental applications. *IEEE Transactions on Geoscience and Remote Sensing*, pages 2316–2329, 2009. doi: 10.1109/TGRS.2009.2012696.

S. D. Miller, W. I. Straka, S. P. Mills, C. D. Elvidge, T. F. Lee, J. Solbrig, A. Walther, A. Heidinger, and S. Weiss. Illuminating the capabilities of the suomi national polar-orbiting partnership (npp) visible infrared imaging radiometer suite (viirs) day/night band. *Remote Sensing*, pages 6717–6766, 2013. doi: 10.3390/rs5126717.

S. D. Miller, D. T. Lindsey, C. J. Seaman, and J. E. Solbrig. Geocolor: A blending technique for satellite imagery. *Journal of Atmospheric and Oceanic Technology*, pages 429–448, 2020. doi: 10.1175/JTECH-D-19-0134.1.

S. D. Miller, Y.-J. Noh, L. D. Grasso, C. J. Seaman, A. Ignatov, A. K. Heidinger, S. Nam, W. E. Line, and B. Petrenko. A physical basis for the overstatement of low clouds at night by conventional satellite infrared-based imaging radiometer bi-spectral techniques. *Earth and Space Science*, 2022. doi: https://onlinelibrary.wiley.com/doi/10.1029/2021EA002137.

Y.-J. Noh, J. M. Haynes, S. D. Miller, C. J. Seaman, A. K. Heidinger, J. Weinrich, M. S. Kulie, M. Niznik, and B. J. Daub. A framework for satellite-based 3d cloud data: An overview of the viirs cloud base height retrieval and user engagement for aviation applications. *Remote Sensing*, page 5524, 2022. doi: 10.3390/rs14215524.

J. E. Overland and B. A. Walter. Gap winds in the strait of juan de fuca. *Monthly Weather Review*, page 2221–2233, 1981. doi: 10.1175/1520-0493(1981)109<2221:GWITSO>2.0.CO;2.

R. N. Patel, S. E. Yuter, M. A. Miller, S. R. Rhodes, L. Bain, and T. W. Peele. The diurnal cycle of winter season temperature errors in the operational global forecast system (gfs). *Geophysical Research Letters*, 2021. doi: 10.1029/2021GL095101.

B. Petrenko, A. Ignatov, Y. Kihai, and A. Heidinger. Clear-sky mask for the advanced clear-sky processor for oceans. *Journal of Atmospheric and Oceanic Technology*, page 1609–1623, 2010. doi: 10.1175/2010JTECHA1413.1.

G. W. Petty. *A First Course In Atmospheric Radiation: Second Edition*. Sundog Publishing, 2006.

S. Pimentel, W. Tse, H. Xu, D. Denaxa, E. Jansen, G. Korres, I. Mirouze, and A. Storto. Modeling the near-surface diurnal cycle of sea surface temperature in the mediterranean sea. *Journal of Geophysical Research: Oceans*, pages 171–183, 2018. doi: 10.1029/2018JC014289.

P. Ricchiazzi, S. Yang, C. Gautier, and D. Sowle. Sbdart: A research and teaching software tool for plane-parallel radiative transfer in the earth's atmosphere. *Bulletin of the American Meteorological Society*, pages 2101–2114, 1998. doi: 10.1175/1520-0477(1998)079<2101:SARATS>2.0.CO;2.

P. Richardson. Florida current, gulf stream, and labrador current. 1st edition of Encyclopedia of Ocean Sciences, volume 2, pp 1054–1064, 2001.

R. Romero-Centeno, J. Zavala-Hidalgo, A. Gallegos, and J. J. O'Brien. Isthmus of tehuantepec wind climatology and enso signal. *Journal of Climate*, pages 2628–2639, 2003. doi: 10.1175/1520-0442(2003)016<2628:IOTWCA>2.0.CO;2.

T. J. Schmit, P. Griffith, J. M. Daniels, S. J. Goodman, and W. J. Lebair. A closer look at the abi on the goes-r series. *Bulletin of the American Meteorological Society*, pages 681–698, 2017. doi: 10.1175/BAMS-D-15-00230.1.

C. Schultz. Satellite salinity data improves gulf stream eddy detection, 2015. URL https://eos.org/research-spotlights/satellite-salinity-data-improves-gulf-stream-eddy-detection.

S. Stanichny, V. Tigny, R. Stanichnaya, and S. Djenidi. Wind driven upwelling along the african coast of the strait of gibraltar. *Geophysical Research Letters*, page L04604, 2005. doi: 10.1029/2004GL021760.

J. Steele, J. Collie, J. Bisagni, D. Gifford, M. Fogarty, J. Link, B. Sullivan, M. Sieracki, A. Beet, D. Mountain, E. Durbin, D. Palka, and W. Stockhausen. Balancing end-to-end budgets of the georges bank ecosystem. *Progress in Oceanography*, pages 423–448, 2007. doi: 10.1016/j.pocean.2007.05.003.

H. G. Stumpf. Satellite detection of upwelling in the gulf of tehuantepec, mexico. *Journal of Physical Oceanography*, pages 383–388, 1975. doi: 10.1175/1520-0485(1975)005<0383:SDOUIT>2.0.CO;2.

R. Sun, S. Moorthi, H. Xiao, and C. Mechoso. Simulation of low clouds in the southeast pacific by the ncep gfs: sensitivity to vertical mixing. *Atmospheric Chemistry and Physics*, pages 12261–12272, 2010. doi: 10.5194/acp-10-12261-2010.

A. Torregrosa, C. Combs, and J. Peters. Goes-derived fog and low cloud indices for coastal north and central california ecological analyses. *Earth and Space Science*, page 46–67, 2016. doi: 10.1002/2015EA000119.

D. W. Townsend, A. C. Thomas, L. M. Mayer, M. A. Thomas, and J. A. Quinlan. *The Sea: The Global Coastal Ocean: Interdisciplinary Regional Studies and Syntheses*. Harvard University Press, 2004.

T. E. Tracey. Measurement and modeling of high energy laser (hel)-droplet interactions. https://apps.dtic.mil/sti/citations/AD1013473, May 2016.

A. Wang and M. F. Modest. Importance of combined lorentz-doppler broadening in high-temperature radiative heat transfer applications. *Journal of Heat Transfer*, pages 858–861, 2004. doi: 10.1115/1.1798951.

D. M. Winker, M. A. Vaughan, A. Omar, Y. Hu, K. A. Powell, Z. Liu, W. H. Hunt, and S. A. Young. Overview of the calipso mission and caliop data processing algorithms. *Journal of Atmospheric and Oceanic Technology*, pages 2310–2323, 2009. doi: 10.1175/2009JTECHA1281.1.

R. Wood. Stratocumulus clouds. *Monthly Weather Review*, page 2373–2423, 2012. doi: 10.1175/MWR-D-11-00121.1.

C. S. Yentsch and N. Garfield. *Oceanography from Space*. Plenum Press, 1981.

J. A. Yoder, S. E. Schollaert, and J. E. O'Reilly. Climatological phytoplankton chlorophyll and sea surface temperature patterns in continental shelf and slope waters off the northeast u.s. coast. *Limnology and Oceanography*, pages 672–682, 2002. doi: https://www.jstor.org/stable/3069156.

J. Yun and K.-J. Ha. Physical processes in sea fog formation and characteristics of turbulent air-sea fluxes at socheongcho ocean research station in the yellow sea. *Frontiers in Marine Science*, 2022. doi: 10.3389/fmars.2022.825973.

J. A. Zhang, E. A. Kalina, M. K. Biswas, R. F. Rogers, P. Zhu, and F. D. Marks. A review and evaluation of planetary boundary layer parameterizations in hurricane weather research and forecasting model using idealized simulations and observations. *Atmosphere*, page 1091, 2020. doi: 10.3390/atmos11101091.

X. Zhou, J. Zhang, and G. Feingold. On the importance of sea surface temperature for aerosol-induced brightening of marine clouds and implications for cloud feedback in a future warmer climate. *Geophysical Research Letters*, 2021. doi: 10.1029/2021GL095896.